JOURNAL OF COMPUTATIONAL PHYSICS 40, 1–35 (1981)

A Linearized 3D Hybrid Code for Stability Studies of Field-Reversed Ion Rings

A. FRIEDMAN* AND R. N. SUDAN

Laboratory of Plasma Studies, Cornell University, Ithaca, New York 14853

AND

J. DENAVIT

Department of Mechanical Engineering and Astronautical Sciences, Northwestern University, Evanston, Illinois 60201

Received May 22, 1979; revised February 7, 1980

A linearized 3D hybrid code, RINGHYBRID, for the study of the low-frequency stability of high-beta equilibria is described. In particular, this code is suitable for application to field-reversed ion rings and mirror plasmas. The code models the development in time of perturbations having a specified azimuthal mode number, l, about an axisymmetric equilibrium state. The equilibrium current is purely azimuthal and is carried entirely by the energetic ion component, which is modeled by discrete simulation particles. This current is consistent with the equilibrium magnetic field and hot-component charge density. In addition to the hot-ion component, a cold uniform density background of ions and a complement of massless electrons are described by fluid equations which incorporate a scalar resistivity. Also presented are verifications of code performance, including tests of cold-plasma normal modes and of plasma return currents arising in response to an azimuthal "drive" current rising linearly with time.

I. INTRODUCTION

In recent years there has been a rebirth of interest in field-reversed configurations, which have the advantage of possessing a region of closed lines for high β plasma confinement surrounded by a region of open lines. This topology requires a relatively simple design for the external magnetic field coils that leads to a major simplification in fusion reactor design. The region of closed lines is produced by internal currents in the plasma. When such currents are force-free the device is known as a spheromak [1]. If the plasma currents flow in the azimuthal direction, only poloidal fields are present and we have a reversed field θ-pinch [2]. A reversed-field mirror [3] is a configuration similar to the θ-pinch except for a lack of axisymmetry introduced by having minimum B quadrupole type coils to provide the external field. The build-up

* Present address: Lawrence Livermore National Laboratory, Livermore, Calif. 94550.

0021-9991/81/030001-35$02.00/0

of field reversal might be achieved by neutral beam injection or by injection of plasma vortices [4].

In the Astron [5] the plasma current for reversing the external field is carried by large orbit energetic charged particles, in contrast to the diamagnetic current of small gyro-radius particles in a θ-pinch or reversed field mirror. A more recent version of this configuration is the ion ring compressor [6, 7]. In this concept a pulse of 10 to 20 MeV ions is injected into a mirror field to form a circulating current of sufficient intensity to reverse the field by its diamagnetic action. By adiabatic magnetic compression the ion energy is increased to a few hundred MeV so that the plasma confined in the closed line region may be heated to thermonuclear fusion conditions. Experimental success in the generation of field-reversed relativistic electron rings [8], in the production of intense pulsed ion beams [9], and in the injection of these beams into mirrors [10] has led to the expectation that field-reversed ion rings will be experimentally realized in the near future.

The issue of the stability of such configurations has therefore attained considerable importance. Even though the observed stability of field reversed electron rings [8] is encouraging, it is not possible to extrapolate the present observations to those envisaged in an ion ring compressor. Stability of field-reversed rings and layers to high-frequency modes can be effectively studied through theoretical analyses because these modes involve short wavelengths, and simplified geometries preserve the essential physics of the mode [11].

With respect to low-frequency stability, results on precessional [12, 13] and tearing [14, 15] modes have been available for some time. The stability of a plasma confined under an assumed-fixed ring [16] has also been treated using the magnetohydrodynamic energy principle. More recently, the kink modes of beams and rings have been examined [17]. A sufficient "energy principle" based on Vlasov formalism has been developed to treat the general low-frequency stability of axisymmetric field-reversed equilibria of arbitrary ion gyro-radius [18].

These analyses have treated "bicycle-tire" (small inverse aspect ratio) and long-layer equilibria, such approximations being necessary to render a simplified analysis tractable. Some general implications of this work are that "thick" bicycle tires would be most stable to the kinking modes, in the sense that stability criteria are satisfied when the parameters of a ring with unit aspect ratio are inserted into the thin ring theory which, however, cannot rigorously be applied in this regime. Similarly, it has been found that infinite layers are stable to precessional and kink modes of sufficiently short axial wavelength [18]. Since a maximum wavelength is imposed by finite layer length, the implication is that finite-length layers might be stable. However, the analysis does not include the destabilizing effect of fieldline curvature at the layer ends. Nonetheless, it is conjectured that a ring with aspect ratio of order unity will represent the most stable configuration; such an aspect ratio is observed in the electron ring experiments.

Theoretical analyses have been unable to approach this regime, as no simple analytical equilibria are known, and approximate treatments are difficult since the inverse aspect ratio cannot be used as an expansion parameter. However, Vlasov

equilibria for rings and mirror plasmas have been found by computational methods [19–21]. One possible approach to the low-frequency stability problem, then, would be to apply a normal mode analysis or an energy principle, as in theoretical treatments, but solving the resulting equations numerically. As mentioned, the magnetohydrodynamic energy principle has been numerically evaluated in the case of a confined plasma and a rigid beam [16].

Our present approach used particle-in-cell and fluid simulation techniques to model realistic equilibria and perturbations about these equilibria. The three-dimensional, linearized hybrid code (RINGHYBRID) we have developed is the subject of this paper. A linearized code [22, 23] has been chosen despite its greater complexity compared with the more usual nonlinear codes, because of several advantages gained through linearization. These include a lower noise level, a reduction in the number of particles and the amount of field and current array storage needed for a particular problem, and somewhat greater flexibility in the model used for the fluid components. Conversely, limitations to the technique include its complexity, the requirement that the equilibria involve at least one ignorable coordinate (i.e., axisymmetry), and the inability to examine nonlinear effects that may lead to saturation of an instability.

We have chosen to utilize a "hybrid" model because we are interested in low-frequency phenomena, and wish to avoid the small temporal and spatial scales involved in electron and ion plasma oscillations and cyclotron motion. Thus, cold background ions (i), which are assumed to uniformly fill the cylindrical chamber, are modeled via a fluid equation. Electrons (e) are also described by a fluid equation, which neglects their inertia and may be considered as an Ohm's law. Collisions between the electrons and background ions are modeled by a constant scalar resistivity, while the hot component (b, for "beam") is collisionless.

Because quasi-neutrality is assumed, and we are interested in low-frequency modes, fields are described by electrodynamic equations excluding displacement current.

The code represents beam ions as finite-size particles, which to lowest order are axisymmetric rings having r, z location and r, θ, z velocities, so that the zero-order state is "two-and-a-half dimensional" [24, 25]. To first order, the beam equations of motion are linearized, with perturbations to particle and field quantities of given toroidal mode number l. Coupling of modes of different l is ruled out by the linearization formalism—stability for each value of l, $l = 0, 1, 2, \ldots$, is examined separately.

Thus, to this order particles are no longer circular rings but are altered in shape by an infinitesimal displacement proportional to $\exp(il\theta)$. Because of the fixed azimuthal dependence, one need only follow first-order displacements and velocities at one "reference" point on the particle. Similarly, field and current quantities are represented by an axisymmetric zero-order part (which may be zero), plus a first-order part varying as $\exp(il\theta)$. The axial, radial, and azimuthal components of the fields and currents are defined on a mesh in the usual manner. The r–z plane is divided into cells, with grid points representing cell centers and all field and current quantities defined on this grid. Since each particle has a finite size, the field applied to each particle is an average of the field values at each of the grid points in cells inter-

secting the particle, the average being weighted according to a smooth particle "shape."

The code at present assumes that the zero-order magnetic field lies entirely in the r–z plane. An external axial (solenoid) field is applied, alone or in conjunction with the field due to an arbitrary set of axisymmetric coils. At present the equilibrium assumes that no plasma currents are flowing, and thus the background plasma pressure gradient must be negligible. To properly represent an arbitrary perturbation, all components of first-order currents and fields are retained.

The structure of this paper is as follows: Section II presents the linearized particle dynamics and describes the particle-moving and current-accumulation part of the code; this is essentially one main module of the code. Section III presents the hybrid model employed, including the fluid equations for the background plasma and the field equations, and describes the manner in which these equations are solved. This represents a second main module of the code, and other plasma models can be incorporated by replacing the appropriate subroutines. Section IV presents a series of tests, based on the normal modes of the background plasma, confirming their correct modeling by the code. Section V presents the application of the code to the problem of plasma return currents across a magnetic field. Finally the Appendix outlines the normalized units used in the code. Subsequent papers will describe the behavior of infinite layers, and will present the application of the code to bicycle-tire and thick ion rings.

II. Particle Dynamics

1. *Representation of Particles*

The beam ions are represented by quasi-circular simulation particles centered on the z axis, with time varying axial positions z and radii r. The exact particle shape is the superposition of a circular (axisymmetric) zero-order configuration and a first-order non-axisymmetric perturbation as shown in Fig. 1. Note that this figure is a "snapshot" of a particle at one given time; it is not a particle orbit, which in general does not close upon itself, and does not necessarily encircle the axis.

Here we examine modes with field variations of the form $\exp(il\theta)$ and the first-order perturbations of the particles must be chosen to maintain this azimuthal dependence of the fields. Such perturbations are defined by choosing on each particle a reference point R, and defining any other point P on the particle by its angle ϕ measured relative to R. As a result of ring rotation, the reference point on each particle is rotated with respect to the x axis by the time-dependent angle α, and since the azimuthal angle θ is measured with respect to the x axis, point P lies at $\theta = \alpha + \phi$. Thus, R and P are the unperturbed locations of the reference and arbitrary points; their perturbed locations are R' and P' defined by the first-order displacements $\boldsymbol{\varepsilon}(R) = \mathbf{OR}' - \mathbf{OR}$ and $\boldsymbol{\varepsilon}(P) = \mathbf{OP}' - \mathbf{OP}$. This representation is repeated for each particle k but the subscript k is omitted to simplify the notation. We now assume that the components of $\boldsymbol{\varepsilon}(P)$ with respect to the coordinate system $(\hat{r}, \hat{\theta}, \hat{z})$ at P have a dependence on ϕ given by $\varepsilon_r(P) = \varepsilon_r(R)\exp(il\phi)$, $\varepsilon_\theta(P) = \varepsilon_\theta(R)\exp(il\phi)$ and $\varepsilon_z(P) =$

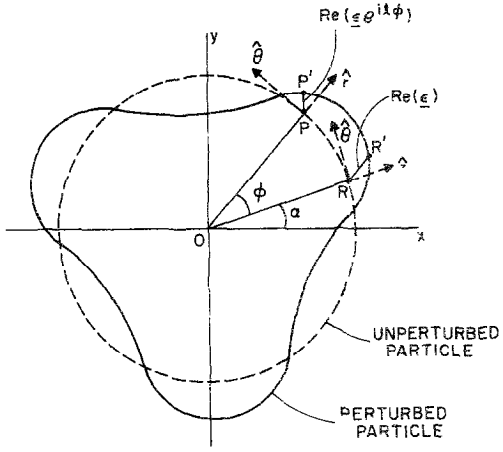

FIG. 1. Illustration of simulation particle showing first-order perturbation $\varepsilon \exp(il\phi)$ to axisymmetric zero-order shape.

$\varepsilon_z(R)\exp(il\phi)$. Note that in Cartesian coordinates this azimuthal dependence would take the form $\varepsilon_x(P) = [\varepsilon_x(R)\cos\phi - \varepsilon_y(R)\sin\phi]\exp(il\phi)$, with similar expressions for $\varepsilon_y(P)$ and $\varepsilon_z(P)$. The displacements $\varepsilon_r(R)$, $\varepsilon_\theta(R)$, $\varepsilon_z(R)$ of the reference point are complex, in general, and the real parts of the resulting expressions must be used. In the code, real quantities are used throughout, writing $\mathbf{PP}' = (\varepsilon_r^{\mathrm{I}}\cos l\phi + \varepsilon_r^{\mathrm{II}}\sin l\phi,$ $\varepsilon_\theta^{\mathrm{I}}\cos l\phi + \varepsilon_\theta^{\mathrm{II}}\sin l\phi,$ $\varepsilon_z^{\mathrm{I}}\cos l\phi + \varepsilon_z^{\mathrm{II}}\sin l\phi)$ so that $\varepsilon_r^{\mathrm{I}}, \varepsilon_r^{\mathrm{II}}$, etc., are followed in time. This is equivalent to keeping track of amplitude and phase information for the components of the displacement. Note that at some instant the node of the perturbation may occur at the reference point which would suffer no displacement, while at $\phi = 90°/l$ around the axis a maximum displacement would occur. For simplicity we will use the complex ε notation in the paper, and occasionally indicate the correspondence to real quantities.

We now proceed to establish that this choice of displacement is consistent with the $\exp(il\theta)$ dependence of the fields, and to prove that it is sufficient to follow only the displacements of the reference point on each particle. Only the $\hat{x}$ components of the equations will be written, since the $\hat{y}$ and $\hat{z}$ components follow similarly. Positions are given by

$$\begin{aligned}(\mathbf{OP}')_x &= (\mathbf{OP})_x + (\mathbf{PP}')_x \\ &= r\cos(\alpha+\phi) + [\varepsilon_r\cos(\alpha+\phi) - \varepsilon_\theta\sin(\alpha+\phi)]\,e^{il\phi}.\end{aligned} \tag{1}$$

With $\theta = \alpha + \phi$ and noting that ϕ is independent of time, the velocities and accelerations are

$$\begin{aligned}(v_{p'})_x = \dot{r}\cos\theta - r\dot{\alpha}\sin\theta + [\dot{\varepsilon}_r\cos\theta - \varepsilon_r\dot{\alpha}\sin\theta \\ - \dot{\varepsilon}_\theta\sin\theta - \varepsilon_\theta\dot{\alpha}\cos\theta]\,e^{il\phi},\end{aligned} \tag{2}$$

and

$$(a_{p'})_x = \ddot{r}\cos\theta - 2\dot{r}\dot{\alpha}\sin\theta - r\ddot{\alpha}\sin\theta - r\dot{\alpha}^2\cos\theta + [\ddot{\varepsilon}_r\cos\theta - 2\dot{\varepsilon}_r\dot{\alpha}\sin\theta - \varepsilon_r\ddot{\alpha}\sin\theta - \varepsilon_r\dot{\alpha}^2\cos\theta - \ddot{\varepsilon}_\theta\sin\theta - 2\dot{\varepsilon}_\theta\dot{\alpha}\cos\theta - \varepsilon_\theta\ddot{\alpha}\cos\theta + \varepsilon_\theta\dot{\alpha}^2\sin\theta]\, e^{il\phi}. \tag{3}$$

The x component of the equation of motion is $m(a_{p'})_x = F_x^0 + F_x^1$, where F_x^0 is the x component of the zero-order electromagnetic force. Because of the azimuthal symmetry of the zero-order fields, $F_x^0 = F_r^0\cos\theta - F_\theta^0\sin\theta$, $F_y^0 = F_r^0\sin\theta + F_\theta^0\cos\theta$ and F_r^0, F_θ^0, F_z^0 are independent of θ. Extracting the zero-order terms and transforming to the local $(\hat{r}, \hat{\theta}, \hat{z})$ system gives

$$m(\ddot{r} - r\dot{\alpha}^2) = F_r^0; \qquad m(r\ddot{\alpha} + 2\dot{r}\dot{\alpha}) = F_\theta^0; \qquad m\ddot{z} = F_z^0. \tag{4}$$

Assuming charge neutrality to zero order, the electromagnetic force is

$$\mathbf{F}^0 = r\dot{\alpha}B_z^0\hat{r} - r\dot{\alpha}B_r^0\hat{z} + (\dot{z}B_r^0 - \dot{r}B_z^0 + E_\theta^0)\hat{\theta}. \tag{5}$$

The first-order motion is similarly given by

$$\begin{aligned} m(\ddot{\varepsilon}_r - \varepsilon_r\dot{\alpha}^2 - \varepsilon_\theta\ddot{\alpha} - 2\dot{\varepsilon}_\theta\dot{\alpha})\, e^{il\phi} &= F_r^1 e^{il\theta} \\ m(\varepsilon_r\ddot{\alpha} + 2\dot{\varepsilon}_r\dot{\alpha} + \ddot{\varepsilon}_\theta - \varepsilon_\theta\dot{\alpha}^2)\, e^{il\phi} &= F_\theta^1 e^{il\theta} \\ m\ddot{\varepsilon}_z e^{il\phi} &= F_z^1 e^{il\theta}, \end{aligned} \tag{6}$$

where $\mathbf{F}^1 e^{il\theta}$ is the force at azimuthal angle θ, e.g.,

$$F_r^1 e^{il\theta} = E_r^1 e^{il\theta} + \delta E_r + r\dot{\alpha}(B_z^1 e^{il\theta} + \delta B_z) - \dot{z}(B_\theta^1 e^{il\theta} + \delta B_\theta) + (\dot{\varepsilon}_\theta + \varepsilon_r\dot{\alpha})\, e^{il\phi}B_z^0, \tag{7}$$

with similar expressions for the $\hat{\theta}$ and $\hat{z}$ components. Here, quantities such as B_z^1 are first-order field amplitudes and quantities such as δB_r are first-order changes in the zero-order fields felt by the particle due to first-order displacements,

$$\boldsymbol{\delta}\mathbf{B} = (\boldsymbol{\varepsilon}e^{il\phi}\cdot\nabla)\,\mathbf{B}^0; \qquad \boldsymbol{\delta}\mathbf{E} = (\boldsymbol{\varepsilon}e^{il\phi}\cdot\nabla)\,\mathbf{E}^0. \tag{8}$$

Noting that at the arbitrary point P we have $\theta = \alpha + \phi$, the phase factor $\exp(il\phi)$ cancels out in the first-order equations of motion, as can be seen by combining Eqs. (6), (7), and (8). These equations yield the linearized equations of motion for ε_r, ε_θ, and ε_z, which are independent of θ or ϕ, and hence the motion of any point P' is known in terms of the motion of R'.

Note in Eq. (6) that the left-hand sides of the first-order equations of motion involve complicated combinations of various components of $\boldsymbol{\varepsilon}$, $\dot{\boldsymbol{\varepsilon}}$, and $\ddot{\boldsymbol{\varepsilon}}$. For this

reason, and to avoid the singularity at the axis, the zero- and first-order positions and velocities are advanced in rectangular coordinates:

$$(m/q)\ddot{\mathbf{r}} = \mathbf{E}^0(\mathbf{r}) + \dot{\mathbf{r}} \times \mathbf{B}^0(\mathbf{r}) \tag{9}$$

$$(m/q)\ddot{\boldsymbol{\varepsilon}} = \underbrace{\mathbf{E}^1(\mathbf{r})\, e^{il\alpha}}_{(1a)} + \underbrace{(\boldsymbol{\varepsilon} \cdot \nabla)\, \mathbf{E}^0(\mathbf{r})}_{(1b)} + \underbrace{\dot{\mathbf{r}} \times [\mathbf{B}^1(\mathbf{r})\, e^{il\alpha} + (\boldsymbol{\varepsilon} \cdot \nabla)\, \mathbf{B}^0(\mathbf{r})]}_{(2a)} + \underbrace{\dot{\boldsymbol{\varepsilon}} \times \mathbf{B}^0(\mathbf{r})}_{(2b)}. \tag{10}$$

However, the field quantities are expressed in cylindrical coordinates and stored on a grid covering the (r, z) plane. They must therefore be interpolated at each time step in terms of r and z, after which they are converted to rectangular coordinates to give the various terms appearing in the right members of Eqs. (9) and (10), $\mathbf{E}^0 = E_\theta^0 \hat{\theta}$, $\mathbf{B}^0 = B_r^0 \hat{r} + B_z^0 \hat{z}$, $\mathbf{E}^1 = E_r^1 \hat{r} + E_\theta^1 \hat{\theta} + E_z^1 \hat{z}$, $\mathbf{B}^1 = B_r^1 \hat{r} + B_\theta^1 \hat{\theta} + B_z^1 \hat{z}$, and

$$\begin{aligned}
(\boldsymbol{\varepsilon} \cdot \nabla)\, \mathbf{E}^0 &= -\varepsilon_\theta \frac{E_\theta^0}{r}\, \hat{r} + \left(\varepsilon_r \frac{\partial E_\theta^0}{\partial r} + \varepsilon_z \frac{\partial E_\theta^0}{\partial z}\right) \hat{\theta} \\
(\boldsymbol{\varepsilon} \cdot \nabla)\, \mathbf{B}^0 &= \left(\varepsilon_r \frac{\partial B_r^0}{\partial r} + \varepsilon_z \frac{\partial B_r^0}{\partial z}\right) \hat{r} + \varepsilon_\theta \frac{B_r^0}{r}\, \hat{\theta} \\
&\quad + \left(\varepsilon_r \frac{\partial B_z^0}{\partial r} + \varepsilon_z \frac{\partial B_z^0}{\partial z}\right) \hat{z},
\end{aligned} \tag{11}$$

where $\hat{r} = \hat{x} \cos\alpha + \hat{y} \sin\alpha$, $\hat{\theta} = -\hat{x} \sin\alpha + \hat{y} \cos\alpha$, $\varepsilon_r = \varepsilon_x \cos\alpha + \varepsilon_y \sin\alpha$ and $\varepsilon_\theta = -\varepsilon_x \sin\alpha + \varepsilon_y \cos\alpha$.

Note that in real notation, $E_r^1(\theta) = E_r^{\mathrm{I}} \cos l\theta + E_r^{\mathrm{II}} \sin l\theta$, and use of trigonometric identities with $\theta = \alpha + \phi$ yields

$$\begin{aligned}
E_r^1(\phi) &= (E_r^{\mathrm{I}} \cos l\alpha + E_r^{\mathrm{II}} \sin l\alpha) \cos l\phi \\
&\quad + (-E_r^{\mathrm{I}} \sin l\alpha + E_r^{\mathrm{II}} \cos l\alpha) \sin l\phi,
\end{aligned} \tag{12}$$

with similar equations for the other components.

2. *Particle-Pushing Algorithms*

Zero-order particle positions and velocities are advanced in Cartesian coordinates using a modified form of the Boris algorithm [26]. Positions are stored at integer timesteps and advanced via a combination of leap-frog and predictor–corrector steps employing velocities at half-integer timesteps. Currents and magnetic fields are defined at integer timesteps and electric (inductive) fields at half-integer times. For the zero order,

$$\mathbf{r}^{N+1} = \mathbf{r}^N + \mathbf{v}^{N+1/2}, \tag{13}$$

and using units for which $\Delta t = 1$ and $\mathbf{B} = \omega_{ci}\Delta t$, our original algorithm yielded $\mathbf{v}^{N+1/2}$ from the sequence

$$\mathbf{v}^{N-1/4} = \mathbf{v}^{N-1/2} + \tfrac{1}{2}\mathbf{E}^{N-1/2}(\mathbf{r}^N), \qquad \mathbf{E}^{N-1/2} = \mathbf{A}^{N-1} - \mathbf{A}^N, \tag{14a}$$

$$\mathbf{v}^* = \mathbf{v}^{N-1/4} + f_1 \mathbf{v}^{N-1/4} \times \mathbf{B}(\mathbf{r}^N), \qquad f_1 = |B|^{-1} \tan|B/2|, \tag{14b}$$

$$\mathbf{v}^{N+1/4} = \mathbf{v}^{N-1/4} + f_2 \mathbf{v}^* \times \mathbf{B}(\mathbf{r}^N), \qquad f_2 = 2f_1/(1 + f_1^2|B|^2), \tag{14c}$$

$$\mathbf{v}^{N+1/2} = \mathbf{v}^{N+1/4} + \tfrac{1}{2}\mathbf{E}^{N+1/2}(\mathbf{r}^N), \qquad \mathbf{E}^{N+1/2} = \mathbf{A}^N - \mathbf{A}^{N+1}, \tag{14d}$$

where $\mathbf{v}^{N-1/4}$ and $\mathbf{v}^{N+1/4}$ denote intermediary values not related to the time-levels $N - 1/4$, $N + 1/4$. This zero-order rotation procedure led to numerical instability of the first-order motion, and was subsequently modified, as discussed below. Note that the above equations are time-centered, although they differ from the original equations of Boris because two half-steps are taken with symmetrical E-fields rather than with a field defined at time level N. Note also that $\mathbf{E}^0 = E_\theta^0 \hat{\theta}$ only, and that close to equilibrium this term will be small; it is, however, important during the initial period of particle injection and relaxation to equilibrium.

This rotation algorithm conserves $v_{||}$ and rotates $\mathbf{v}_\perp$ through the appropriate angle.

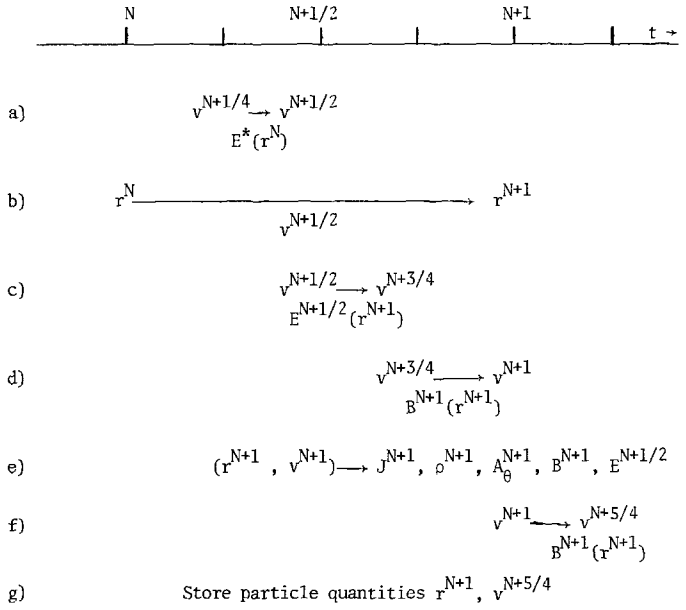

FIG. 2. Schematic of zero-order timestep. Note that: (i) On the first pass, only steps (a)–(e) are performed. E^* is $E^{N-1/2}$ on the first pass, and $E^{N+1/2}$ thereafter. (ii) Steps (f) and (g) are only performed on the last pass, after all zero- and first-order calculations are done. (iii) When first-order calculations are also being performed, step (e) is omitted; the other steps must be repeated since the first-order calculation requires r^{N+1}, v^{N+1}, and possibly r^N. (iv) If fields are frozen and $E_\theta^0 = 0$, steps (a) and (c) may be omitted. Particle-splitting coefficients need only be evaluated at r^{N+1} unless the plasma model in use dictates otherwise.

A half-angle rotation, obtained by setting $f_1 = |B|^{-1} \tan |B/4|$, is used to split the rotation steps Eqs. (14b) and (14c) so that velocities defined at integer steps may be obtained for purposes of current accumulation. The sequence of operations carried out at each time step is summarized in Fig. 2. Half-electric fields are stored on the mesh and Eq. (14d) is applied first to obtain $\mathbf{v}^{N+1/2}$, because $\mathbf{E}^{N+1/2}$ is known only at this time. For the predictor step we use $\mathbf{E}^{N-1/2}$. We then advance positions to obtain $\mathbf{r}^{N+1}$, and proceed with Eqs. (14a), (14b), and (14c) with N incremented to $N+1$ and a half-push to obtain $\mathbf{v}^{N+1}$. The currents are computed at this point to allow a reevaluation of $\mathbf{A}^{N+1}$ and the iteration is repeated. Finally, on the last corrector pass only, Eqs. (14b) and (14c) are applied again to complete the rotation. Thus, we store $\mathbf{r}^{N-1}$, $\mathbf{v}^{N+1+1/4}$ at the end of each time step. Typically, a single corrector step is used.

After a quiet equilibrium has been achieved, fields are usually "frozen," that is, we set $E_\theta^0 = \partial/\partial t\, \mathbf{B}^0 = \partial/\partial t\, A_\theta^0 = 0$, and the zero-order current-finding and field-solving steps are omitted. In this case the zero-order part of the code amounts to a simple integration of particle motion along unperturbed orbits in an equilibrium field, the

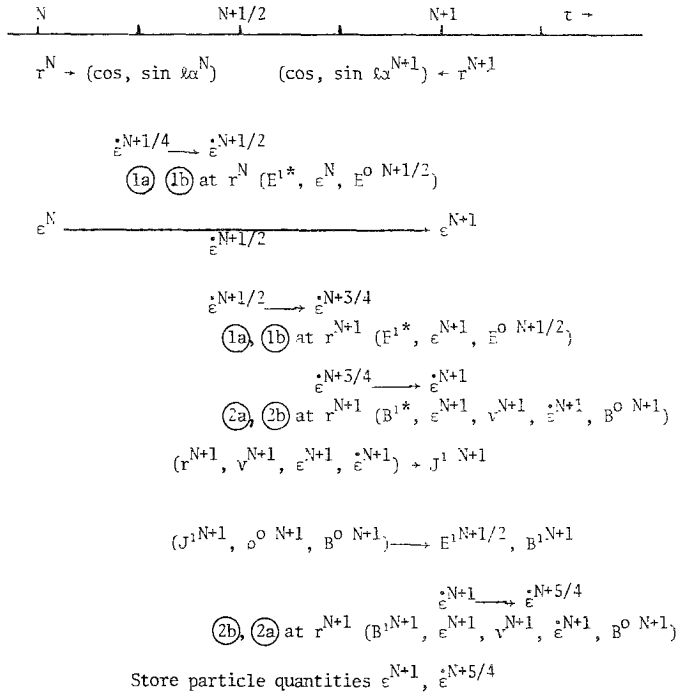

FIG. 3. Schematic of general first-order timestep. Note that: (i) E^{1*} is $E^{1N-1/2}$ on first pass. $E^{1N+1/2}$ thereafter. B^{1*} is B^{1N} on first pass, B^{1N+1} thereafter. (ii) Steps (h) and (i) are only performed on the last pass. On the last pass, steps (f) and (g) are omitted. (iii) Typically, three passes through the first-order particle calculations are performed; the first uses the previous E^1 and B^1, providing a predictor for the fields derived from J^1; the second acts as a corrector for the fields; the last uses the corrected fields to advance the particles. (iv) $E^{1N+1/2}$ is obtained either from $(A^{1N} - A^{1N+1})$ or from $(E^{1N+1} + E^{1N})/2$. depending upon the plasma model employed.

zero-order beam charge density ρ^0, needed to give the local excess electron density, also being "frozen." These orbits are generally nonlaminar and chaotic.

A similar procedure is employed in the solution of the first-order equations, as shown in Fig. 3. The zero-order timestep having been completed, $\mathbf{r}$, $\mathbf{v}$, and $\mathbf{B}^0$ are known at times N and $N+1$, while $\mathbf{E}^0$ is known at time $N+1/2$. The "B-like" last term in the right member of Eq. (10), $\dot{\boldsymbol{\varepsilon}} \times \mathbf{B}^0(\mathbf{r})$, which is similar to the term $\dot{\mathbf{r}} \times \mathbf{B}^0$ of Eq. (9), yields a rotation of $\dot{\boldsymbol{\varepsilon}}$ carried out by Eqs. (14b) and (14c) of the Boris algorithm. The remaining "E-like" terms of Eq. (10) are substituted for $\mathbf{E}$ in Eqs. (14a) and (14d) to complete the update of $\dot{\boldsymbol{\varepsilon}}$ in a time-centered manner. As mentioned earlier, this adaptation of the Boris algorithm was found to give a numerical instability of the first-order motion in infinite layer runs, for particles whose radial betatron period is an integral number of timesteps. This instability is due to the inconsistent manner in which the "B-like" term $\dot{\boldsymbol{\varepsilon}} \times \mathbf{B}^0(r)$ is treated using the correction factor $f_1 = |\mathbf{B}|^{-1} \tan |\mathbf{B}/2|$, while the corresponding "E-like" term $\dot{\mathbf{r}} \times (\boldsymbol{\varepsilon} \cdot \nabla)\, \mathbf{B}^0(r)$ is advanced without such a correction. The latest version of the code treats all first-order terms consistently by a modification of this algorithm obtained

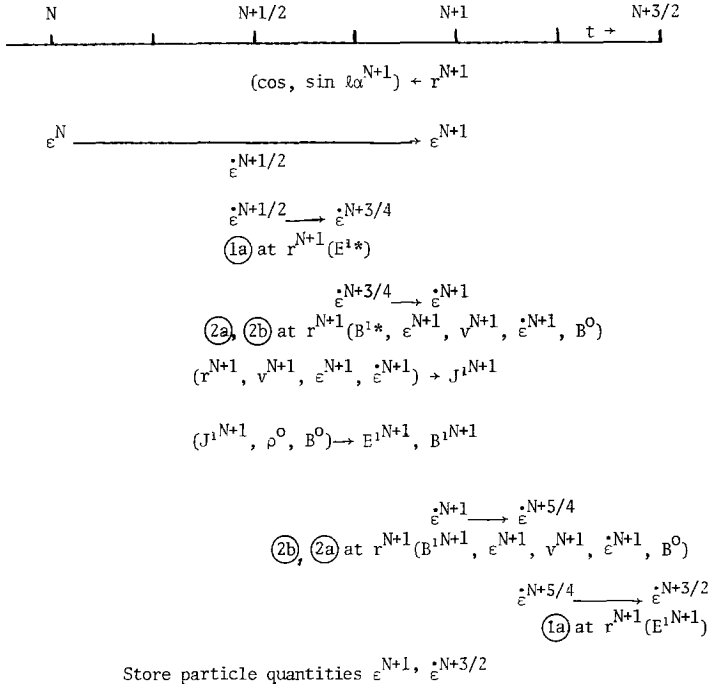

FIG. 4. Schematic of first-order timestep when E^1 is defined at integral times, and zero-order fields are frozen. Note that: (i) E^{1*} is E^{1N} on first pass, E^{1N+1} thereafter. B^{1*} is B^{1N} on first pass, B^{1N+1} thereafter. (ii) Steps (g) and (h) are only performed on the last pass. On the last pass, steps (e) and (f) are omitted. (iii) As in the scheme of Fig. 3, typically three passes are used. (iv) The forces 2*a*, 1*a* in steps (g) and (h) yield the same velocity increments as those of steps (c) and (d), but are applied after the rotations (force 2*b*). Only one set of splitting coefficients need be calculated (at r^{N+1}).

by setting $f_1 = 1/2$ and $f_2 = (1 + |B|^2/4)^{-1}$ in Eqs. (14b) and (14c), for both zero-order and first-order rotations. This scheme preserves particle energy, but does not rotate the particle velocity by the exact angle, thus introducing a small error in the resulting cyclotron frequency. The computations described in this article use the earlier method and, in the cases which have been repeated with the new methods, the behavior was essentially unchanged when timestep-resonant particles are absent.

The first-order step also involves an iteration since first-order fields at time $N+1$ are not known at the beginning of the timestep. For the algorithm shown, $\mathbf{E}^1$ is defined at time $N+1/2$ and is given by backward-averaging $\mathbf{E}^1$ at time $N+1$ (obtained from the plasma model to be described in Section III) with $\mathbf{E}^1$ at N. The algorithm is thus applicable to other plasma models in which $\mathbf{E}^1$ is derived from $\partial \mathbf{A}^1/\partial t$ and to equilibria which involve zero-order electric fields. It is, however, rather slow since substep (b) requires calculation of the entire set of weights associated with the shape function and its spatial derivatives at time level N.

For the plasma model described in Section III, a more efficient algorithm, depicted in Fig. 4, is usable when zero-order fields are frozen. The term $(\boldsymbol{\varepsilon} \cdot \nabla)\,\mathbf{E}^0$ is zero, and $\mathbf{E}^1$ is centered at time $N+1$; thus, substep (b) in Fig. 3 has been moved to the end of the previous timestep, after substep (h) of Fig. 3. It yields the same velocity increment as substep (d) of Fig. 3, but is applied after the rotation. Weights are only calculated at time level $N+1$.

3. *Current Density of the Discrete Ion Component*

Since a particle consists of many points, each defined by its angle ϕ with respect to the reference point R, the charge density distribution of particle k is the sum of contributions from individual points,

$$\rho_k(r, \theta, z) = \frac{q_k}{2\pi r} \int_0^{2\pi} \delta[r - r_k(\phi)]\, \delta[\theta - \theta_k(\phi)]\, \delta[z - z_k(\phi)]\, d\phi, \tag{15}$$

where q_k is the total charge on the particle and $r_k(\phi)$, $\theta_k(\phi)$, $z_k(\phi)$ define the particle shape parametrically. Similarly, the current of particle k is:

$$\mathbf{J}_k(r, \theta, z) = \frac{q_k}{2\pi r} \int_0^{2\pi} \delta[r - r_k(\phi)]\, \delta[\theta - \theta_k(\phi)]\, \delta[z - z_k(\phi)]\, \mathbf{v}_k(\phi)\, d\phi, \tag{16}$$

where $\mathbf{v}_k(\phi)$ is the velocity of that element of particle k situated at angle ϕ relative to the reference point. We expand $\mathbf{r}_k(\phi)$ and $\mathbf{v}_k(\phi)$:

$$\begin{aligned}
r_k(\phi) &= r_k^0 + \varepsilon_{rk} e^{il\phi}, \\
\theta_k(\phi) &= \theta_k^0 + \varepsilon_{\theta k} e^{il\phi}/r_k^0, \\
z_k(\phi) &= z_k^0 + \varepsilon_{zk} e^{il\phi}, \\
v_{rk}(\phi) &= \dot{r}_k^0 + (\dot{\varepsilon}_{rk} - \varepsilon_{\theta k}\dot{\alpha}_k)\, e^{il\phi}, \\
v_{\theta k}(\phi) &= r_k^0 \dot{\alpha}_k + (\dot{\varepsilon}_{\theta k} + \varepsilon_{rk}\dot{\alpha}_k)\, e^{il\phi}, \\
v_{zk}(\phi) &= \dot{z}_k^0 + \dot{\varepsilon}_{zk} e^{il\phi}.
\end{aligned} \tag{17}$$

Before Eqs. (15) and (16) can be used to extract zero and first order current densities, they must be modified to account for the finite size of the particles. This is achieved by introducing a grid in the r, z plane with discrete grid points (or cell centers) at r_j and z_i and replacing the δ functions of Eqs. (15) and (16) by finite radial and axial shape functions $S_r(r)$ and $S_z(z)$. With these modifications, the current contribution of particle k to cell (j, i) is

$$\mathbf{J}_{k,j,i}(\theta) = \frac{q_k}{2\pi r_j} \int_0^{2\pi} S_r[r_j - r_k(\phi)]\, S_z[z_i - z_k(\phi)]\, \delta[\theta - \theta_k(\phi)]\, \mathbf{v}_k(r^0, \phi)\, d\phi, \quad (18)$$

where $\mathbf{v}_k(r^0, \phi)$ is now the velocity of that part of the finite-size particle at unperturbed radius r^0. For rigid rotation of the points comprising the superparticle, v_θ^0 is proportional to radius and there is no shear to the flow. Because v_θ^0 differs for different points of the superparticle, the algorithms for weighting J_θ^0 and ρ^0 to the grid will differ. The expression (17) for $v_{\theta k}(r^0, \phi)$ must be multiplied by r^0/r_k^0, where r_k^0 is the nominal radial location of the particle. A detailed discussion of appropriate expressions for S_r and S_z is presented in the next section.

Substituting Eqs. (17) into Eq. (18), and expanding the shape functions and velocity in Taylor series yields for the $\hat{r}$ component of the current due to a set of particles $k = 1,..., N$,

$$J_{ri,j}^0 = \frac{1}{2\pi r_j} \sum_{k=1}^{N} q_k S_r S_z \dot{r}_k^0 \int_0^{2\pi} \delta[\theta - \theta_k^0(\phi)]\, d\phi, \quad (19)$$

to zero order, and

$$\begin{aligned} J_{ri,j}^1 e^{il\theta} = {} & \frac{1}{2\pi r_j} \sum_{k=1}^{N} q_k \left[\dot{\varepsilon}_{rk} S_r S_z + \dot{r}_k^0 \left(\varepsilon_{rk} \frac{\partial S_r}{\partial r_k^0} S_z \right.\right. \\ & \left.\left. + \varepsilon_{zk} S_r \frac{\partial S_z}{\partial z_k^0} \right) \right] \int_0^{2\pi} e^{il\phi} \delta[\theta - \theta_k^0(\phi)]\, d\phi \\ & + \frac{1}{2\pi r_j} \sum_{k=1}^{N} q_k S_r S_z \dot{r}_k^0 \left[\int_0^{2\pi} \delta \left(\theta - \theta_k^0 - \frac{\varepsilon_{\theta k}}{r_k^0} e^{il\phi} \right) d\phi - 1 \right], \end{aligned} \quad (20)$$

to first order. Here the shape functions and their derivatives are evaluated at the zero-order positions, $S_r = S_r(r_j - r_k^0)$ and $S_z = S_z(z_i - z_k^0)$. In the left member of Eq. (20), the azimuthal dependence of the first-order current, given by $\exp(il\theta)$, has been separated from its radial and axial dependence, given by $J_{ri,j}^1$. Since $\theta_k^0 = \alpha_k + \phi$, the integral over ϕ in Eq. (19) gives unity and the integral over ϕ in the first term in the right member of Eq. (20) gives $\exp[il(\theta - \alpha_k)]$. The integral in the last term of Eq. (20) yields

$$1 + \int_0^{2\pi} \frac{\varepsilon_{\theta k}}{r_k^0} e^{il\phi} \frac{\partial}{\partial \phi} \delta(\theta - \alpha_k - \phi)\, d\phi,$$

or, after integration by parts, $1 - il(\varepsilon_{\theta k}/r_k)\exp[il(\theta - \alpha_k)]$. Note that $\mathbf{v}_k$ is a vector field when one considers a finite-size superparticle, so that the vectorial expansion of $(\boldsymbol{\varepsilon} \cdot \nabla)\mathbf{v}$ must be used.

Noting that J_r^0 and J_z^0 are essentially zero near equilibrium, the relevant charge and current densities are

$$
\begin{aligned}
\rho_{i,j}^0 &= \frac{1}{2\pi r_j} \sum_{k=1}^{N} q_k S_r S_z \\
J_{\theta i,j}^0 &= \frac{1}{2\pi} \sum_{k=1}^{N} \frac{q_k}{r_k} S_r S_z v_{\theta k}, \\
J_{ri,j}^1 &= \frac{1}{2\pi r_j} \sum_{k=1}^{N} q_k e^{-il\alpha_k} \left\{ \left(\dot{\varepsilon}_{rk} - \frac{il\varepsilon_{\theta k} v_{rk}}{r_k} \right) S_r S_z \right. \\
&\quad \left. + v_{rk}\varepsilon_{zk} S_r S_z' + v_{rk}\varepsilon_{rk} S_r' S_z \right\}, \\
J_{\theta i,j}^1 &= \frac{1}{2\pi} \sum_{k=1}^{N} \frac{q_k}{r_k} e^{-il\alpha_k} \left\{ \left(\dot{\varepsilon}_{\theta k} - \frac{\varepsilon_{\theta k} v_{rk}}{r_k} - \frac{il\varepsilon_{\theta k} v_{\theta k}}{r_k} \right) S_r S_z \right. \\
&\quad \left. + v_{\theta k}\varepsilon_{zk} S_r S_z' + v_{\theta k}\varepsilon_{rk} S_r' S_z \right\}, \\
J_{zi,j}^1 &= \frac{1}{2\pi r_j} \sum_{k=1}^{N} q_k e^{-il\alpha_k} \left\{ \left(\dot{\varepsilon}_{zk} - \frac{il\varepsilon_{\theta k} v_{zk}}{r_k} \right) S_r S_z \right. \\
&\quad \left. + v_{zk}\varepsilon_{zk} S_r S_z' + v_{zk}\varepsilon_{rk} S_r' S_z \right\},
\end{aligned} \tag{21}
$$

where $S_r' \equiv \partial S_r/\partial r_k$, $S_z' \equiv \partial S_z/\partial z_k$.

Since particle coordinates and velocities are computed in Cartesian coordinates, these quantities need to be converted to cylindrical coordinates before substitution into Eqs. (21). Refering to Eq. (2), and the associated equation for $(v_p)_y$ gives

$$
\begin{aligned}
v_{rk} &= v_{xk}^0 \cos\alpha_k + v_{yk}^0 \sin\alpha_k, \\
v_{\theta k} &= -v_{xk}^0 \sin\alpha_k + v_{yk}^0 \cos\alpha_k,
\end{aligned} \tag{22}
$$

for the zero-order velocities, and

$$
\begin{aligned}
\dot{\varepsilon}_{rk} - \varepsilon_{\theta k} v_{\theta k}^0 / r_k^0 &= v_{xk}^1 \cos\alpha_k + v_{yk}^1 \sin\alpha_k, \\
\dot{\varepsilon}_{\theta k} + \varepsilon_{rk} v_{\theta k}^0 / r_k^0 &= -v_{xk}^1 \sin\alpha_k + v_{yk}^1 \cos\alpha_k,
\end{aligned} \tag{23}
$$

for the first-order velocities.

Note that in terms of real quantities,

$$
\dot{\varepsilon}_{rk} = \dot{\varepsilon}_{rk}^{\mathrm{I}} \cos l\phi + \dot{\varepsilon}_{rk}^{\mathrm{II}} \sin l\phi, \tag{24}
$$

the first term in the expression for J_r^1 becomes proportional to

$$(\dot{\varepsilon}_{rk}^{\mathrm{I}} \cos l\alpha_k - \dot{\varepsilon}_{rk}^{\mathrm{II}} \sin l\alpha_k) \cos l\theta + (\dot{\varepsilon}_{rk}^{\mathrm{I}} \sin l\alpha_k + \dot{\varepsilon}_{rk}^{\mathrm{II}} \cos l\alpha_k) \sin l\theta,$$

corresponding to a rotation back to the x axis through an angle $l\alpha_k$. Similarly, for the third term in J_θ^1,

$$\frac{l}{r_k}\{[-\varepsilon_{\theta k}^{\mathrm{II}} \cos l\alpha_k - \varepsilon_{\theta k}^{\mathrm{I}} \sin l\alpha_k] \cos l\theta + [\varepsilon_{\theta k}^{\mathrm{I}} \cos l\alpha_k - \varepsilon_{\theta k}^{\mathrm{II}} \sin l\alpha_k] \sin l\theta\}.$$

Expressions equivalent to these can also be derived by considering $J^1 \propto n^1 v^0 + n^0 v^1$ as if each particle were a fluid stream using Bobroff's formalism [27]. Alternatively, we can consider point particles in θ and pass to finite-aximuthal-extent through an integration over unperturbed azimuthal location. These derivations may in some ways be simpler than our derivation, but one must be careful to note that **v** is not the same for all points of the superparticle. The terms in our current densities may be interpreted as being due to either first-order velocities or first-order charge densities.

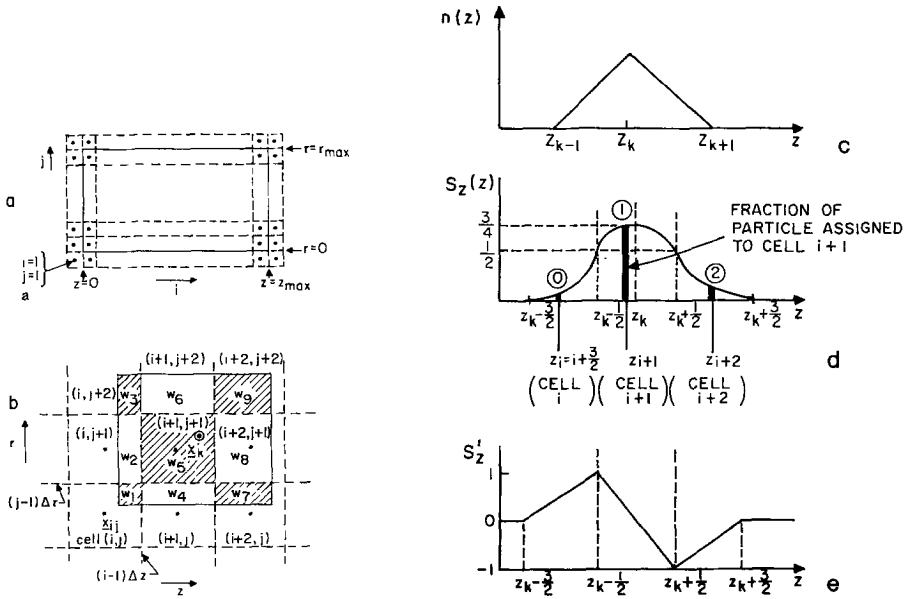

FIG. 5. Particle shapes and interpolation scheme. (a) The r, z plane divided into cells, with grid points representing cell centers. Heavy lines indicate the physical boundaries of the system. (b) A particle with finite radial and axial extent intersecting nine cells. Splitting coefficients $W_1, \ldots, W_9$ are shown. (c) Particle density in real space as a function of z (r is similar). (d) Shape function showing fraction of particle's charge assigned to each of the axial columns of cells it intersects, corresponding to the density of (c). (e) Derivative of the axial shape function.

4. *Particle Shapes and Interpolation*

The r, z plane is divided into cells of size Δr by Δz, and grid points are assumed to represent cell centers. The cells are arranged as shown in Fig. 5a with guard cells outside the boundaries of the system, and potentials, fields, densities, and currents all defined at the same grid points. Each finite-size particle has a specified density profile as a function of r and z, specified by the shape functions $S_r(r)$ and $S_z(z)$. The value of a field applied to a given particle k is a weighted average of the field values at grid points in all cells intersected by the particle.

We define cell (i, j) to be the *left lower* cell intersecting the particle, and note that nine cells with indices i, $i+1$, $i+2$ and $j, j+1, j+2$ intersect each particle with the shape function utilized (Fig. 5b).

Currents and charge contributed by a particle are distributed among the same nine cells. To obtain the current density, the product (charge × velocity) in each cell is first accumulated by summing contributions from all intersecting particles, and then divided by the volume of the cell, $2\pi r_j \Delta r \Delta z$.

Since first-order currents depend on the derivatives of the shape functions, see Eqs. (20), shape functions with continuous derivatives must be used to avoid excessive grid noise in the first-order calculation. The particle charge density in real space as a function of z (with $\Delta z = 1$) is shown in Fig. 5c, and the same charge distribution is used in the radial direction. This corresponds to the particle shape function, or spline, shown in Fig. 5d, giving the fraction of the particle's charge assigned to each cell. At points 0, 1, 2 this function takes on values:

$$S(0) = \tfrac{1}{2}(z_i - z_k + 3/2)^2 = \tfrac{1}{2}(i - z_k)^2,$$
$$S(1) = \tfrac{3}{4} - (z_i - z_k + 1)^2 = \tfrac{3}{4} - (i - z_k - \tfrac{1}{2})^2,$$
$$S(2) = \tfrac{1}{2}(z_i - z_k + 1/2)^2 = \tfrac{1}{2}(i - z_k - 1)^2,$$

satisfying the normalization $S(0) + S(1) + S(2) = 1$ and the continuity condition: $S(0)\,|_{z_k = z_i + 1/2} = S(1)\,|_{z_k = z_i + 3/2}$.

Setting $i \equiv [z_k + 1], j \equiv [r_k + 1]$, $r_q \equiv j - r_k$, and $z_q \equiv i - z_k$, where heavy brackets indicate the greatest-integer function, the shape function values at appropriate cells in z and r are:

$$i: W_{z0} = 0.5 z_q^2; \qquad j: W_{r0} = 0.5 r_q^2;$$
$$i+1: W_{z1} = 0.75 - (z_q - 0.5)^2; \qquad j+1: W_{r1} = 0.75 - (r_q - 0.5)^2;$$
$$i+2: W_{z2} = 0.5(z_q - 1)^2; \qquad j+2: W_{r2} = 0.5(r_q - 1)^2;$$

from which the splitting coefficients indicated in Fig. 5b are $W_1 = W_{z0} W_{r0}$, $W_2 = W_{z0} W_{r1}, \ldots, W_9 = W_{z2} W_{r2}$.

The derivative of the shape function S_z' (or S_r'), illustrated in Fig. 5e, takes the following values at the appropriate cells,

$$i: W'_{z0} = -z_q; \qquad j: W'_{r0} = -r_q;$$
$$i+1: W'_{z1} = 2(z_q - 1/2); \qquad j+1: W'_{r1} = 2(r_q - 1/2);$$
$$i+2: W'_{z2} = 1 - z_q; \qquad j+2: W'_{r2} = 1 - r_q;$$

From these values and the corresponding values of shape functions themselves the splitting coefficients corresponding to the terms $S'_z S_r$ in Eq. (20) are $W_{10} = W'_{z0} W_{r0}$,..., $W_{18} = W'_{z2} W_{r2}$, and the splitting coefficients corresponding to the terms $S_z S'_r$ are $W_{19} = W_{z0} W'_{r0}$,..., $W_{27} = W_{z2} W'_{r2}$. Note that because of the continuity of the derivative shape functions the first-order currents do not undergo any sharp changes as a particle moves from cell to cell.

The derivative-shape functions are used not only in the calculation of first-order currents, but also in the evaluation of those first-order forces on the particle involving $(\boldsymbol{\varepsilon} \cdot \nabla)\, \mathbf{B}_0$. It is important to use the *same* shape function in all calculations, and the correct derivative shape function, since a first-order displacement should provide the same change in a field quantity that would be produced by an infinitesimal zero-order displacement. For example, if S'_r were not in fact the radial derivative of S_r, then "precession" of the displaced reference point would proceed at a different rate than would precession of the zero-order reference point.

III. Field Computations

1. *Zero-Order Field Solution*

Zero-order fields B^0_r, B^0_z, and E^0_θ are given by centered spatial and temporal derivatives of the vector potential A^0_θ. Space charge, and radial and axial net currents, are assumed negligible near equilibrium, and, consistent with the low-pressure background plasma assumed, no zero-order azimuthal plasma current is included. In terms of the dimensionless units defined in the Appendix, the field equation solved is

$$\nabla^2 A^0_\theta - \frac{A^0_\theta}{r^2} = -J^0_\theta + \sigma^0\, \partial A^0_\theta / \partial t, \tag{25}$$

where A^0_θ refers to the self-field, exclusive of the external field, σ^0 is a constant, a backward difference is used for $\partial A^0_\theta / \partial t$. The purpose of the term $-\sigma^0\, \partial A^0_\theta / \partial t$ is to introduce damping into the system in a manner which causes collective oscillations of the zero-order ring to diminish with time. This effect, which has proven useful for the generation of "quiet" equilibria, is described elsewhere [28]. When an approximate equilibrium is reached (true time-independence is never reached because of the finite number of particles) the $\sigma^0\, \partial A^0_\theta / \partial t$ term becomes negligible.

As indicated erlier, the computations are usually simplified by freezing the zero-order magnetic fields B^0_r and B^0_z and setting the zero-order electric field E^0_θ to zero

before the first-order perturbations are initialized. Computations in which the small time variations of the zero-order fields are retained have verified that they do not affect the code results significantly.

Boundary conditions are imposed on A_θ^0 during the solution by requiring the self-field part of A_θ^0 to be zero at $r=0$ and $r=r_w$. To this end, values of A_θ^0 in the appropriate guard cells are set equal to the negative of the values in the appropriate physical cells. Periodic or metallic wall boundary conditions are imposed in z. The field equation is solved by over-relaxation; more efficient methods are possible but are not necessary, since the first-order particle-pushing dominates the calculation.

The use of guard cells allows the application of fields to particles near the system boundaries to follow the same procedure as for particles in the interior of the system. Furthermore, when a particle "spills over" into a guard cell its currents can be accumulated in the usual manner; currents added to axial guard cells are simply transferred to the physical cell one system length away, to satisfy the periodicity requirement. "Sticky" walls absorb particles within a half cell of the outer wall at $r=r_w$; currents near $r=0$ all go into the smallest-radius physical cell ($j=2$). In many cases, when equilibrium has been reached and fields are "frozen" there is no longer any need to check particle boundary conditions. With the exception of some axially long equilibria, where periodicity may have to be enforced, particles normally no longer reach the radial or axial boundaries of the system.

2. *First-Order Field Solution*

The numerical study of the low-frequency ($\omega \ll \omega_{ce}$) stability of ion rings requires a representation of the background plasma, coupled to the ring ions, and capable of supporting hydromagnetic waves. In the model considered here, this background plasma consists of cold ions (i) and electrons (e) of sufficient number density to maintain quasi-neutrality. These cold components are described by fluid equations and the first-order fields $\mathbf{E}^1$ and $\mathbf{B}^1$ are evaluated in terms of Maxwell's equations. Since only low frequencies are considered, and the system is assumed quasi-neutral. both transverse and longitudinal components of the displacement current are neglected in Ampere's law.

The fluid part of the code is complete in itself, and can support linearized cold 3D hydromagnetic waves in cylindrical geometry, as shown in Section IV. The model used for the plasma is similar to models introduced by Byers *et al.*, but does not use the vector potential [29]. The ring ions, or hot component, are coupled to the background plasma in three ways: (a) the equilibrium ring current significantly alters the zero-order field, (b) the beam ions increase the local electron density, and (c) first-order beam currents provide a source term in Ampere's law.

Consistent with the treatment of ring ions, the background fluid equations are linearized. and thermal effects, electron inertia, and collisions with the ring ions are neglected.

In terms of the dimensionless variables defined in the Appendix, and omitting the primes, the model equations are

$$
\begin{aligned}
0 &= -(\mathbf{E} + \mathbf{v}_e \times \mathbf{B}) - \rho_i \eta (\mathbf{v}_e - \mathbf{v}_i), \\
\partial \mathbf{v}_i / \partial t &= (Z/m)(\mathbf{E} + \mathbf{v}_i \times \mathbf{B}) - (Z/m)(-\rho_e)\, \eta (\mathbf{v}_i - \mathbf{v}_e), \\
-\rho_e &= \rho_i + \rho_b, \\
\nabla \times \mathbf{B} &= \mathbf{J}_e + \mathbf{J}_i + \mathbf{J}_b, \\
\nabla \times \mathbf{E} &= -\partial \mathbf{B} / \partial t,
\end{aligned} \tag{26}
$$

where ρ_e, ρ_i, and ρ_b are the charge densities of electrons, background ions, and beam ions, respectively, and η is a constant scalar resistivity arising from collisions between background ions and electrons. According to the definitions of the Appendix, Z and m denote the charge and mass of the background ions relative to the charge and mass of the beam ions. Note that the longitudinal (curl free) part of J_{total} is zero, as appropriate for low-frequency oscillations. This set of equations is solved for the first-order electric field by rewriting the electron momentum equation using quasi-neutrality, $\mathbf{J}_{i,e} = \rho_{i,e} \mathbf{v}_{i,e}$, and Ampere's law,

$$
\begin{aligned}
\mathbf{E} = {} & \frac{\mathbf{B}^0}{\rho_i + \rho_b} \times (\mathbf{J}_b + \mathbf{J}_i - \nabla \times \mathbf{B}) \\
& + \frac{\rho_i}{\rho_i + \rho_b} \eta \left(-\mathbf{J}_b + \nabla \times \mathbf{B} + \frac{\rho_b}{\rho_i} \mathbf{J}_i \right),
\end{aligned} \tag{27}
$$

and systematically eliminating $\mathbf{B}$ and $\mathbf{J}_i$ from this equation. Letting a tilde ($\sim$) denote a quantity defined at the previous integral timestep, $\mathbf{B}$ is obtained from Faraday's law,

$$
\mathbf{B} = -\tfrac{1}{2} \nabla \times \mathbf{E} - \tfrac{1}{2} \nabla \times \tilde{\mathbf{E}} + \tilde{\mathbf{B}}, \tag{28}
$$

and $\mathbf{J}_i$ is obtained from the ion momentum equation,

$$
\partial \mathbf{J}_i / \partial t = (Z/m) \{ \rho_i \mathbf{E} + \mathbf{J}_i \times \mathbf{B}^0 - \eta \rho_i [-\mathbf{J}_b + \nabla \times \mathbf{B} + (\rho_b / \rho_i)\, \mathbf{J}_i] \}. \tag{29}
$$

As the zero-order field is time-independent, $\mathbf{B}$ is substituted for in terms of $\mathbf{E}, \tilde{\mathbf{E}}, \tilde{\mathbf{B}}$ using Eq. (28), and Eq. (29) yields the finite difference equation

$$
\begin{aligned}
& \mathbf{J}_i + (Z/2m)\, \mathbf{B}^0 \times \mathbf{J}_i + (Z/2m)\, \rho_b \eta \mathbf{J}_i \\
& \quad = (Z/2m)\, \rho_i \mathbf{E} + (Z/4m)\, \rho_i \eta \nabla \times \nabla \times \mathbf{E} + \mathbf{S},
\end{aligned} \tag{30}
$$

where

$$
\begin{aligned}
\mathbf{S} = {} & \tilde{\mathbf{J}}_i + (Z/2m) \{ -\mathbf{B}^0 \times \tilde{\mathbf{J}}_i - \rho_b \eta \tilde{\mathbf{J}}_i + \rho_i \tilde{\mathbf{E}} \\
& + \tfrac{1}{2} \rho_i \eta \nabla \times \nabla \times \tilde{\mathbf{E}} - 2 \rho_i \eta \nabla \times \tilde{\mathbf{B}} + \rho_i \eta \tilde{\mathbf{J}}_b + \rho_i \eta \mathbf{J}_b \},
\end{aligned} \tag{31}
$$

consists entirely of quantities defined at the previous timestep, excepting the last term. Solving Eq. (30) for $\mathbf{J}_i$ gives

$$\mathbf{J}_i = \frac{\vec{G}}{D}\left[(L\mathbf{E}) + \mathbf{S}\right] \tag{32}$$

where

$$\begin{aligned}
\vec{G} &= \begin{bmatrix} (1+\varepsilon)^2 + b_r^2 & (1+\varepsilon)\, b_z & b_z b_r \\ -(1+\varepsilon)\, b_z & (1+\varepsilon)^2 & (1+\varepsilon)\, b_r \\ b_z b_r & -(1+\varepsilon)\, b_r & (1+\varepsilon)^2 + b_z^2 \end{bmatrix}, \\
D &= (1+\varepsilon)[(1+\varepsilon)^2 + b_z^2 + b_r^2], \\
L &= \frac{Z\rho_i}{2m}\left[1 + \frac{\eta}{2}\nabla\times\nabla\times\right],
\end{aligned} \tag{33}$$

with $b_z = ZB_z^0/2m$, $b_r = ZB_r^0/2m$ and $\varepsilon = (Z/2m)\,\rho_b\eta$. Source terms which depend on $\mathbf{J}_b$ are separated from those containing only quantities known from the previous timestep by defining

$$\tilde{\mathbf{P}} \equiv \frac{2m}{Z\rho_i}\mathbf{S} - \eta\mathbf{J}_b, \tag{34}$$

and reassembling the various terms of Eq. (27) yields the final equation:

$$\begin{aligned}
\mathbf{E} = \frac{\rho_i}{\rho_b + \rho_i}\Bigg\{\Bigg[&\frac{\mathbf{B}^0}{2\rho_i}\times\nabla\times\nabla\times\mathbf{E} + \left(\frac{Z\mathbf{B}^0}{2m}\right)\times\frac{\vec{G}}{D}\left(\mathbf{E} + \frac{\eta}{2}\nabla\times\nabla\times\mathbf{E}\right) \\
&- \frac{\eta}{2}\nabla\times\nabla\times\mathbf{E} + \eta\frac{Z\rho_b}{2m}\frac{\vec{G}}{D}\left(\mathbf{E} + \frac{\eta}{2}\nabla\times\nabla\times\mathbf{E}\right)\Bigg] + \mathbf{W}_b + \mathbf{W}_p\Bigg\},
\end{aligned} \tag{35}$$

where

$$\begin{aligned}
\mathbf{W}_b &= \frac{\mathbf{B}^0}{\rho_i}\times\mathbf{J}_b - \eta\mathbf{J}_b + \eta\left(\frac{Z\mathbf{B}^0}{2m}\right)\times\frac{\vec{G}}{D}\mathbf{J}_b + \eta^2\frac{Z\rho_b}{2m}\frac{\vec{G}}{D}\mathbf{J}_b, \\
\mathbf{W}_p &= \frac{\mathbf{B}^0}{2\rho_i}\times\nabla\times\nabla\times\tilde{\mathbf{E}} - \frac{\eta}{2}\nabla\times\nabla\times\tilde{\mathbf{E}} - \frac{\mathbf{B}^0}{\rho_i}\times\nabla\times\tilde{\mathbf{B}} \\
&\quad + \eta\nabla\times\tilde{\mathbf{B}} + \left(\frac{Z\mathbf{B}^0}{2m}\right)\times\frac{\vec{G}}{D}\tilde{\mathbf{P}} + \eta\frac{Z\rho_b}{2m}\frac{\vec{G}}{D}\tilde{\mathbf{P}},
\end{aligned}$$

and $\tilde{P}$ explicitly given by

$$\begin{aligned}
\tilde{\mathbf{P}} = \frac{2m}{Z\rho_i}\tilde{\mathbf{J}}_i - \frac{\mathbf{B}^0}{\rho_i}\times\tilde{\mathbf{J}}_i - \eta\frac{\rho_b}{\rho_i}\tilde{\mathbf{J}}_i + \tilde{\mathbf{E}} \\
+ \frac{\eta}{2}\nabla\times\nabla\times\tilde{\mathbf{E}} - 2\eta\nabla\times\tilde{\mathbf{B}} + \eta\tilde{\mathbf{J}}_b.
\end{aligned} \tag{36}$$

The term $\mathbf{W}_p$ in Eq. (35) constitutes a source term, which is constant during each timestep. The term $\mathbf{W}_b$ is a source term which is updated at each pass through the particles in a predictor–corrector iteration. The first term in square brackets in Eq. (35) is an operator on $\mathbf{E}$ which could be brought to the left member of the equation and $\mathbf{E}$ solved for by matrix inversion. However, an analysis of the relative size of the terms in this equation shows that for the parameter regime of interest (ρ_i large, $B^0 \propto \Delta t$ small) the pivot term $\mathbf{E}_{i,j}$ in the left member of Eq. (35), with a coefficient of unity, will be dominant over all other $\mathbf{E}$ terms. The timestep limitation imposed by this condition is usually less severe than the requirement of properly representing the self-field betatron motion of the hot component. A simple relaxation iteration is therefore used, replacing $\mathbf{E}_{i,j}$ on the LHS by $\omega_b \times (\text{RHS}) + (1 - \omega_b) \times (\mathbf{E}_{i,j}$, last iterate), where ω_b is the overrelaxation parameter, using checkerboard overrelaxation. Convergence for a typical problem is very rapid, reaching residuals comparable to machine roundoff in about 20 iterations on a 24×24 mesh.

One subtle point is that $\nabla \times \tilde{\mathbf{B}}$ should not be directly evaluated in computing the source term. Since $\mathbf{B}$ is found by centered difference operations on $\mathbf{E}$, $\nabla \times \mathbf{B}$ involves an operator on E which is a *five*-point stencil in each direction, and is inconsistent with other terms where $\nabla \times \nabla \times \mathbf{E}$, which is a *three*-point stencil, appears explicitly. We thus retain an effective $\nabla \times \mathbf{B}$ (total current) set of arrays via a recurrence on $\nabla \times \nabla \times \mathbf{E}$:

$$\nabla \times \mathbf{B}^N = -\tfrac{1}{2} \nabla \times \nabla \times \mathbf{E}^N - \nabla \times \nabla \times \mathbf{E}^{N-1} - \nabla \times \nabla \times \mathbf{E}^{N-2} - \cdots - \nabla \times \nabla \times \mathbf{E}^1 - \tfrac{1}{2} \nabla \times \nabla \times \mathbf{E}^0 + \nabla \times \mathbf{B}^0, \tag{37}$$

Failure to do so leads to a short-wavelength numerical instability.

Boundary conditions imposed on the iteration are purely geometrical at $r = 0$. The symmetry of each azimuthal mode number l fixes the boundary condition there. At r_w we impose $E_\theta = E_z = 0$, corresponding to an infinitely-conducting wall, by setting $E_{\theta,z}$ (guard cell) $= -E_{\theta,z}$ (last physical cell). For nonaxisymmetric modes with nonuniform external magnetic field it is necessary to evaluate the terms $\partial/\partial r[\partial E_r/\partial z]$ and $\partial/\partial r[\partial E_r/\partial \theta]$ in the last physical cell. Since neither of these is second-order in E_r, and we do not wish to impose a nonphysical boundary condition on E_r, it is appropriate to use uncentered radial derivatives in evaluating these quantities in the last physical cell only. It is equivalent, and computationally faster, to set E_r (guard cell) to the appropriate linear combination of E_r values in the last two physical cells, so that in the iteration the last physical cell can be treated like any other. Before this was realized, a variety of other boundary conditions on E_r were employed, setting E_r (guard cell) $= C_1 \cdot E_r$ (last physical cell), where $-1 \leqslant C_1 \leqslant 1$. The choice of any of these boundary conditions on E_r had little effect on plasma behavior, because the value of E_r in the last physical cell is only very weakly affected by the value of E_r in the guard cell. The $l = 1$ cold plasma normal mode runs described in Section IV actually used $C_1 = 1.0$, though several were repeated using the uncentered derivative formulation as a check.

Boundary conditions in z may be specified to be either periodic or similar to those at the outer wall.

After $\mathbf{E}$ is calculated, $\mathbf{B}$ is obtained from Eq. (28) and used with $\mathbf{E}$ in the next particle iteration. $\mathbf{J}_i$ is calculated from Eq. (32) as it is needed in the calculation of the source term for the next timestep. Extensive use of multipurpose scratch arrays is necessary.

IV. Normal Modes of the Background Plasma

The correct functioning of the first-order plasma model is verified by introducing waves of known dispersion relation into the system. No ion ring is set up in these computations, but the discrete particles usually representing the beam are initialized throughout the plasma with their zero-order velocity set to zero. In the absence of resistivity, these particles should behave in a manner representative of the cold background ions. In particular, the beam current $\mathbf{J}_b$ should be proportional to $\mathbf{J}_i$ in any given cell, the constant of proportionality being ρ_b/ρ_i. If this ratio is negligibly small, the beam particles act as test particles only, but if $\rho_b/\rho_i = 1$, equal currents should arise from discrete and fluid ion components, and $-\rho_e = \rho_b + \rho_i = 2\rho_i$ should obtain. This procedure serves to verify much of the first-order particle-advancing and current-accumulating performed by the code.

The normal modes of a cold plasma in a cylindrical geometry have been obtained by Bernstein and Trehan [30]. Instead of their vacuum boundary condition, we impose conditions corresponding to the existence of a metallic wall at $r = r_w$.

$$\frac{-\omega^2}{v_A^2}\mathbf{B} = \nabla \times \{[(\nabla \times \mathbf{B}) \times \hat{z}] \times \hat{z} + iW[(\nabla \times \mathbf{B}) \times \hat{z}]\}. \tag{38}$$

where $\mathbf{B}$ denotes the first-order magnetic field, $v_A = B^0/(4\pi n_i m_i)^{1/2}$ is the Alfvén speed, $W = \omega/\Omega$, $\Omega = \omega_{ci} = eB^0/m_i c$, and B^0 is the external magnetic field, assumed uniform. After considerable but straightforward manipulation, elimination of B_r and B_θ from Eq. (38) yields Bessel's quation for B_z, from which

$$B_z = B_1 J_l(\nu r), \tag{39}$$

where B_1 is a constant and the radial wave number ν is given by

$$\nu^2 = -\Lambda^{-1}(k_{||}^2 - \omega^2/v_A^2 - k_{||}^2 W^2)^{-1}, \tag{40}$$

where

$$\Lambda = [(k_{||}^2 - \omega^2/v_A^2)^2 - k_{||}^4 W^2]^{-1}. \tag{41}$$

The boundary condition $B_r(r_w) = 0$ is applied by substituting B_z from Eq. (39) into the r component of Eq. (38), which yields

$$v_m^2 \Lambda \frac{l}{r_w} W \frac{\omega^2}{v_A^2} J_l(v_m r_w) = -\frac{\partial}{\partial r} J_l(v_m r) \bigg|_{r_w}. \tag{42}$$

This equation may be solved to obtain the discrete set v_m, $m = 1, 2,...$, of allowable values of v after ω has been expressed in terms of v by solving Eq. (40),

$$2\omega^2 = v_A^2[v^2(1 + k_{||}^2 v_A^2/\Omega^2) + k_{||}^4 v_A^2/\Omega^2 + 2k_{||}^2] \pm \{[v^2(1 + k_{||}^2 v_A^2/\Omega^2) + k_{||}^4 v_A^2/\Omega^2 + 2k_{||}^2]^2 v_A^4 - 4[k_{||}^2 v_A^4 v^2 + k_{||}^4 v_A^4]\}^{1/2}. \tag{43}$$

Note that this expression is independent of l, and that (40) may be solved for W^2 to yield the more familiar dispersion relation:

$$W^2 = (1 - \omega^2/k_{||}^2 v_A^2)[1 - \omega^2/(v_A^2[k_{||}^2 + v_m^2])]. \tag{44}$$

For $W^2 \ll 1$ this immediately yields the fast and slow MHD modes.

Defining $\omega_p \equiv \omega_{pi} = c\Omega/v_A$ and using the Bessel function identity, $J_p'(x) = -px^{-1}J_p(x) + J_{p-1}(x)$, we obtain the equation for the roots v_m in the form:

$$0 = \frac{J_{l-1}(v_m r_w)}{J_l(v_m r_w)} + \frac{l}{v_m r_w} \left\{ \frac{(\omega^3/\Omega^3)(v_m^2 c^2/\omega_p^2)}{[(k_{||}^2 c^2/\omega_p^2) - (\omega^2/\Omega^2)]^2 - (k_{||}^4 c^4/\omega_p^4)(\omega^2/\Omega^2)} - 1 \right\}. \tag{45}$$

This can be solved in general form; for purposes of code verification we specialize to two cases: (i) $l = 0$, $k_{||} \neq 0$, and (ii) $l \neq 0$, $k_{||} = 0$. The former verifies the action of the finite difference operations in r and z; the latter checks the behavior of nonaxisymmetric modes.

A. $l = 0$, $k_{||} \neq 0$ *Case*

For this case, which is discussed in a different manner by Stix [31], the boundary condition reduces to $J_1(v_m r_w) = 0$, from which $v_1 \simeq 3.832/r_w$, $v_2 \simeq 7.016/r_w$, $v_3 \simeq 10.173/r_w$,.... For a given radial wave number v_m, specification of $k_{||}$ and choice of the sign in Eq. (43) yields ω. Combining Ampere's law and the ion momentum equation, to obtain $\mathbf{v}$, and using $\mathbf{E} = -(\mathbf{v} \times \mathbf{B}^0 - \mathbf{J} \times \mathbf{B}^0/ne)/c$, yields

$$\frac{iE_r}{E_\theta} = \frac{\omega^3/\Omega^3}{(\omega^2/\Omega^2)[1 + (k_{||}^2 c^2/\omega_p^2)] - (k_{||}^2 c^2/\omega_p^2)}, \tag{46}$$

and $E_r, E_\theta \propto J_1(v_m r)$. The presence of the i in Eq. (46) indicates that E_r and E_θ are out of phase by 90°.

Finite Δt correction. Letting a tilde denote a value at the previous timestep, an equation of the form $\partial \mathbf{B}/\partial t = f(\mathbf{E})$, where f is a linear operator, yields $(\mathbf{B} - \tilde{\mathbf{B}})/\Delta t = f(\mathbf{E} + \tilde{\mathbf{E}})/2$. Since $\tilde{\mathbf{B}} = \mathbf{B} \exp(i\omega \Delta t)$ and $\tilde{\mathbf{E}} = \mathbf{E} \exp(i\omega \Delta t)$, this finite-difference equation yields $\mathbf{B}[1 - \exp(i\omega \Delta t)]/\Delta t = [1 + \exp(i\omega \Delta t)] f(\mathbf{E})/2$, and it follows that

the operator $\partial/\partial t$ is not $-i\omega$ but $-i\omega_{ef}$, where $\omega_{ef} = (2/\Delta t)\tan(\omega\,\Delta t/2)$, where ω is obtained from the analytic dispersion relation. Since only the fluid ion component is treated in a fully implicit manner by the code, this heuristic analysis does not correctly treat the discrete particle ion component.

The wave in real variables. Since all variables used in the code are real, all amplitudes and phases must be expressed in terms of real quantities. Setting

$$\mathbf{E} = \{\hat{r}\,|E_r|\cos(k_{||}z - \omega_{ef}t) - \hat{\theta}\,|E_\theta|\sin(k_{||}z - \omega_{ef}t)\}\,J_1(v_m r),$$

Faraday's law yields:

$$B_r = \frac{ck_{||}}{\omega_{ef}}\,|E_\theta|\sin(k_{||}z - \omega_{ef}t)\,J_1(v_m r),$$

$$B_\theta = \frac{ck_{||}}{\omega_{ef}}\,|E_r|\cos(k_{||}z - \omega_{ef}t)\,J_1(v_m r),$$

$$B_z = \frac{cv_m}{\omega_{ef}}\,|E_\theta|\cos(k_{||}z - \omega_{ef}t)\,J_0(v_m r),$$

where $|E_r|, |E_\theta|$ are related according to Eq. (46), and the ion momentum equation gives

$$J_{i\theta} = \frac{-\omega_p^2}{4\pi}\frac{\omega_{ef}}{\Omega^2 - \omega_{ef}^2}\left[-|E_\theta| + \frac{\Omega}{\omega_{ef}}|E_r|\right]\cos(k_{||}z - \omega_{ef}t)\,J_1(v_m r),$$

$$J_{ir} = \frac{\omega_p^2}{4\pi}\frac{\omega_{ef}}{\Omega^2 - \omega_{ef}^2}\left[-\frac{\Omega}{\omega_{ef}}|E_\theta| + |E_r|\right]\sin(k_{||}z - \omega_{ef}t)\,J_1(v_m r).$$

The wave is initialized by setting these quantities, with $t = 0$, into the tilde arrays.

Damping. The resistive term included in the code damps hydromagnetic waves. For small ω, the damping is weak and the dissipationless normal mode structure may be retained as a good approximation. By analogy with the infinite-medium case the damping rate is: $\gamma \simeq \eta c^2\omega^2/8\pi v_A^2$, which in dimensionless units is $\eta\omega^2/2v_A^2$.

Examples.. The examples shown use a 26×26 mesh (including guard cells). A "diagnostic cell," from which field and current are stored for subsequent plotting as functions of time, was chosen to have indices $i_{\text{diagn}} = 15(z)$, $j_{\text{diagn}} = 13(r)$.

Let $n_{||}$ denote the number of wavelengths in the system in the axial direction; m is twice the number of "wavelengths" in the radial direction, i.e., the number of radial nodes of E_θ plus one.

The first example shown is for the case $m = 3$, $n_{||} = 2$, and the positive sign in front of the radical in Eq. (43). The dimensionless magnetic field magnitude is $B_0 = \omega_{ci}\,\Delta t = .68$, giving a cyclotron period $\tau_{ci} \simeq 9.24$ timesteps, and the plasma density, Zn_i, in dimensionless units is $\rho_i = 10$. Test particles were set up with infinitesimal

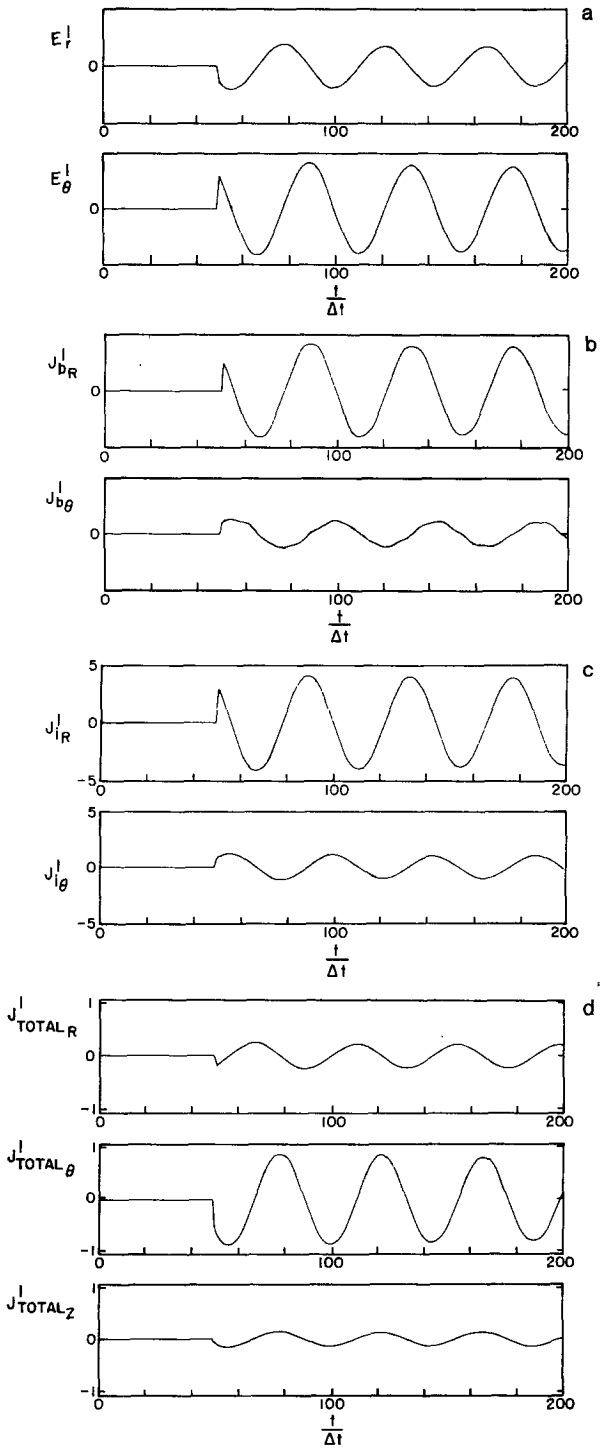

FIG. 6. Quantities in diagnostic cell as functions of time for the first $l = 0$ cold plasma normal mode example. (a) Radial and azimuthal electric field components. (b) Radial and azimuthal discrete-test-particle ion current components. (c) Radial and azimuthal fluid ion current components. (d) Radial, azimuthal, and axial total current components.

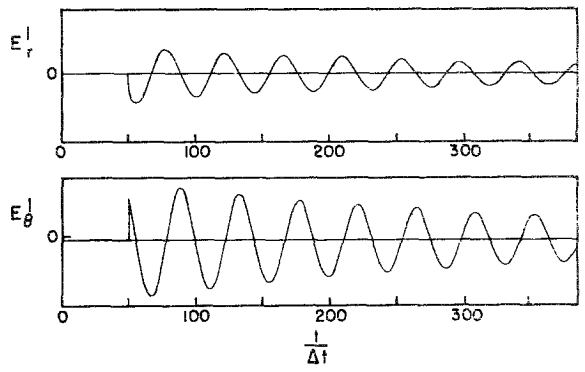

FIG. 7. Radial and azimuthal electric field components in diagnostic cell as functions of time for the second cold-plasma normal mode example, showing the effect of nonzero resistivity.

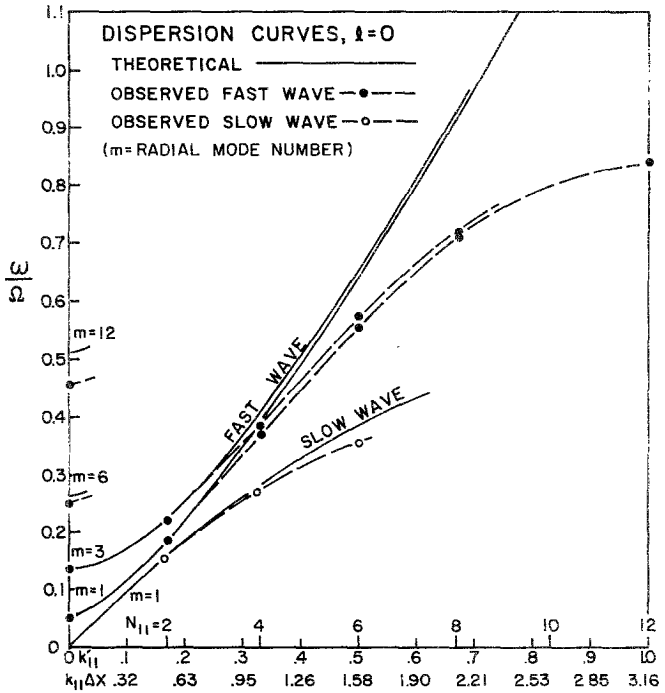

FIG. 8. Ideal-theoretical and observed $l = 0$ fast- and slow-wave frequencies as functions of $k_{||}' = k_{||}c/\omega_{pi}$, plotted for various radial mode numbers m. For these runs $Zn_i = 10.0$. Also shown on the abscissa are the corresponding values of $k_{||}\Delta x$ and $n_{||}$, the number of axial wavelengths in the system.

charge ($\rho_b/\rho_i \cong 1.74 \times 10^{-20}$ in the diagnostic cell), and the wave was initialized at timestep 50. The analytic wave frequency is calculated to be $\omega = .1794$, and the finite-Δt wave frequency is $\omega_{ef} = .1497$, corresponding to a period of 42 timesteps. Figure 6a shows radial and azimuthal electric fields in the diagnostic cell as functions of time. These quantities oscillate with a period very close to 42 timesteps, and as expected, the radial field is seen to lead the azimuthal field by 90°. The radial and azimuthal currents due to the discrete ion test particles, shown in Fig. 6b, are proportional to the fluid-ion currents (at the same diagnostic cell) in the ratio ρ_b/ρ_i, see Fig. 6c. Finally Fig. 6d shows total r, θ, and z currents in the diagnostic cell as a function of time. Observe that electrons move axially, consistent with charge neutrality since ions, because of inertia, have a different radial motion than electrons.

The second example shows the effect of introducing a dimensionless resistivity $\eta = .01$. Retaining the same values of other parameters, the theoretically predicted damping rate is $\gamma = 2.4 \times 10^{-3}$ corresponding to a $1/e$ time of 410 timesteps. The electric field in the diagnostic cell, plotted as a function of time in Fig. 7, shows a damping at the rate $\gamma_{\text{obs}} \simeq 2.9 \times 10^{-3}$. The discrepancy seems to be due to imperfect initialization of the normal mode, resulting in a small wave component corresponding to the negative sign in Eq. (43), introducing a beat, which, over the observation interval, appears as additional "damping." In addition, it should be noted that the predicted damping rate is not exact since $\omega/\Omega = 0.22$ is not truly small.

Dispersion Curves. Figure 8 shows ideal and observed wave frequencies as functions of $k'_{||} = k_{||} c/\omega_{pi}$ and m, for runs like the above. For long wavelengths little numerical dispersion error is evident, while for short wavelengths the wave frequency

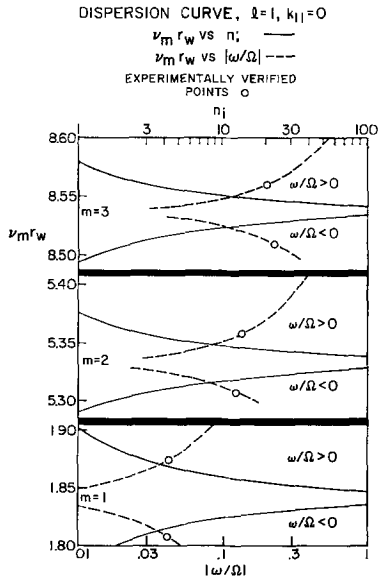

FIG. 9. $\nu_m r_w$ as a function of Zn_i (solid curves) and of ω/Ω for the $l = 1$, $k_{||} = 0$ normal modes. Circles indicate the point on each branch which was verified experimentally.

is appreciably less than gridless theory predicts, due to $k_{||}\Delta x$ being greater than unity.

B. $l \neq 0$, $k_{||} = 0$ *Case*

In the limit of infinite-length modes, Eq. (43) gives $\omega/\Omega = \pm v_m c/\omega_p$, and Eq. (45) yields:

$$J_{l-1}(v_m r_w)/J_l(v_m r_w) \pm \frac{lc}{\omega_p r_w} - \frac{l}{v_m r_w} = 0, \tag{47}$$

where ω_p/c becomes $(Zn_i)^{1/2}$ in dimensionless units. While in the $l = 0$ case we specified Zn_i and solved for v_m, in the present case it is easier to specify $v_m r_w$ and solve for Zn_i since this does not require inverting the ratio of Bessel functions. Several values of $v_m r_w$ give the same Zn_i, and the plot of Zn_i as a function of $v_m r_w$, shown in Fig. 9, was constructed to select values of $v_m r_w$ giving a value of Zn_i close to that desired. The lower signs were used in Eq. (47) for Zn_i, and in computing the corresponding value of ω. The mode structure must be implemented in real variables as in the $l = 0$ case. Using dimensionless variables (with $Z = 1$, $m_b/m_i = 1$) and omitting the argument $(v_m r)$ of the Bessel functions, the wave fields and currents are

$$E_r = \frac{B^0 B_1}{n_i}\left[\frac{-B^0 l}{r\omega} J_l - v_m J_l'\right][\cos\omega t \cos l\theta + \sin\omega t \sin l\theta],$$

$$E_\theta = \frac{B^0 B_1}{n_i}\left[\frac{B^0 v_m}{\omega} J_l' + \frac{l}{r} J_l\right][\cos\omega t \sin l\theta - \sin\omega t \cos l\theta],$$

$$E_z = 0,$$

$$B_r = B_\theta = 0,$$

$$B_z = B_1[\cos\omega t \cos l\theta + \sin\omega t \sin l\theta] J_l,$$

$$J_{ir} = -\frac{B^0 B_1 v_m}{\omega}[\sin\omega t \cos l\theta - \cos\omega t \sin l\theta] J_l',$$

$$J_{i\theta} = \frac{B^0 B_1}{\omega}\frac{l}{r}[\cos\omega t \cos l\theta + \sin\omega t \sin l\theta] J_l,$$

$$J_{iz} = 0.$$

These equations are used, with $t = 0$, to initialize the tilde arrays. Note that n_i here includes contributions from both fluid and discrete components. Note also that J_{ir} cannot be zero at the wall in the two-fluid formulation used.

Example. The results of a computation with $l = 1$, $B^0 = -0.196$, and $v_m r_w = 8.56$, corresponding to a density $n_i = 3.189$, and to the third radial mode ($m = 3$) with this density, appear in Fig. 10. Here, J_{ir} has two internal radial nodes, and a small value at the wall, about 5 % of its peak value. This computation was done with half of the

ions modeled by the fluid, and half by discrete ions, with one particle at each radial interface between cells, and particle charges chosen to give uniform density. There were 26 cells in r (including guard cells) and, since this problem is axially uniform, only 6 cells (the minimum allowed by the code) were used in Z. The theoretically predicted wave frequency is -3.92×10^{-2}, corresponding to a period of 160 timesteps. The radial and azimuthal currents of fluid ions in the diagnostic cell ($j = 13$) are plotted as functions of time in Fig. 10a, while Fig. 10b shows the currents due to discrete ions. The two are seen to be very nearly equal, and the wave period to be approximately correct. The run was continued until timestep 700 with no deviation from the harmonic behavior observed.

Summary of Runs. Figure 9 indicates the point on each of the six dispersion curves which was verified experimentally. These results, and those corresponding to two higher radial mode numbers, are described in Table I. Note that a radial mode number $m = 20$ corresponds to 10 radial "wavelengths" in the system.

Other wave tests were performed using very short radial wavelengths, without true normal mode initialization, as a test of code stability. By this means the desirability of using $\nabla \times \nabla \times \mathbf{E}$ rather than $\nabla \times \mathbf{B}$, in the source term of Eq. (35), was discovered. With the revised source term short wavelengths do not induce instability.

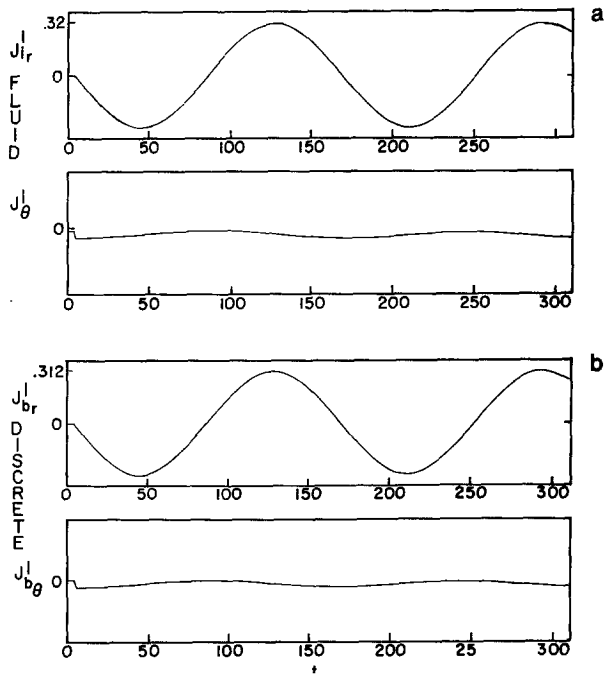

FIG. 10. Quantities in diagnostic cell as functions of time for the $l = 1$ cold plasma normal mode example. (a) Radial and azimuthal components of the fluid ion current. (b) Radial and azimuthal components of the discrete ion current.

TABLE I

Summary of $l = 1$, $k_{\|} = 0$ Runs[a]

m	$v_m r_w$	n_i	ω/Ω analyt.	$\|\omega/\Omega\|$ obs.
3	8.56	3.18928	.200	.199
3	8.51	2.56818	−.221	.221
2	5.357	2.86682	.132	.132
2	5.307	3.10717	−.125	.125
1	1.874	3.25139	.0433	.0432
1	1.808	3.16118	−.0424	.0426
12	36.88	17.42465	−.368	.334
20	62.025	32.16720	−.456	.339

[a] The last column shows the absolute value of the observed normalized wave frequency because only the wave period, and not the polarization, were measured; the wave was initialized with the correct polarization.

V. Plasma Return Currents across a Magnetic Field

As a further test of our algorithm, we have applied RINGHYBRID to the problem of plasma return currents induced by a driving layer current rising linearly with time. This problem is relevant to the buildup of ion current field reversal in ion ring and field reversed-mirror experiments.

The slab geometry analog of this problem has been solved analytically by Berk and Pearlstein [32], and slab geometry simulations have been carried out by Byers *et al.* [29]. Also, the problem has been modeled by Condit [33] in an annular cylindrical geometry, employing an inner ("cantilever") conductor and specifying the thickness of the plasma region to be small compared with its radius. In contrast, the present model contains no inner conductor, and so cylindrical-geometry effects are more pronounced than in the previous work. Another difference is present between this work and the aforementioned simulation studies. Since the driving current is due to a second ion component, as it increases the local electron density should also increase to preserve charge neutrality. However, we assume this excess electron density to be negligible. This amounts to the specification of a low-charge-density, high-velocity current sheet.

The most important feature of the analytic solution to the slab problem is that the plasma return current does not continue to rise indefinitely, even though the driving sheet current does. Only for a time on the order of a Alfven transit time ($\approx r_w/2V_z$) is the net current essentially zero. For longer times, the plasma current oscillates with an amplitude much less than that of the drive current. It is this characteristic behavior which is modeled in our simulations.

We consider a one-dimensional limit ($l = 0$, $\partial/\partial z = 0$) of RINGHYBRID, with 48 cells in the radial direction. The drive current is included by adding an extra source term to the $J_{b\theta}^{(1)}$ array. This current is entirely a first-order quantity ($J^{(0)}$ is zero for all

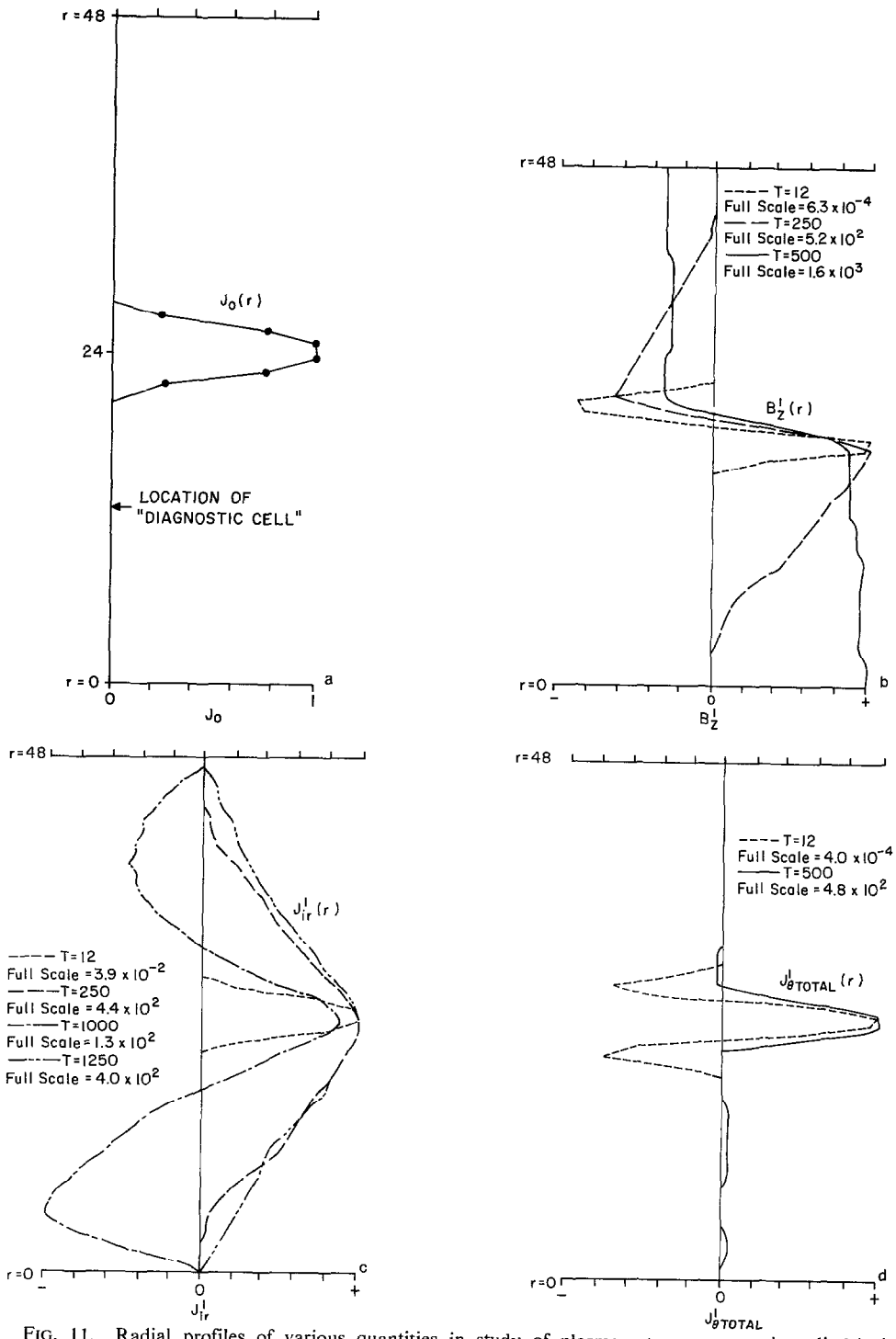

FIG. 11. Radial profiles of various quantities in study of plasma return currents in cylindrical geometry. (a) "Drive" current. (b) First-order magnetic field at $t = 12, 250, 500$. (c) First-order radial ion current at $t = 12, 250, 1000, 1250$. (d) First-order total azimuthal current at $t = 12, 500$.

time), so that the linearized response is obtained using the full hybrid model described in Section II. We specify J_θ (drive) to be zero for $t \leqslant 11$, then J_θ (drive) $= J_0(r)[t-11]$, where the drive current profile $J_0(r)$ is illustrated in Fig. 11a. Specifically, for the cells with center at $r = 23.5$ and 24.5, $J_0 = 1$; for cells at $r = 22.5$ and 25.5, $J_0 = .75$; and for cells at 21.5 and 26.5, $J_0 = .25$. This smooth current profile was chosen to avoid the generation of short wavelengths in the system. The cyclotron period τ_{ci} was chosen to be 80 timesteps, the Alfven velocity $v_A = .0785$ cells/timestep, and the diagnostic cell for time-histories was located at $r = 12.5$. The simulation was run for 3000 timesteps.

Magnetic field profiles at various times are shown in Fig. 11b. The profile at $t = 12$ shows the strong effect of the plasma return current. The first-order magnetic field is localized to the layer region. By $t = 250$, the wavefront has moved out $v_A(250-11) = 19$ cells, and by $t = 500$ the magnetic field profile is essentially that associated with the drive current. At later times the same profile (with a linearly increasing amplitude) is observed.

Profiles of the radial ion current at various times appear in Fig. 11c. These profiles evidence the presence of non-growing Alfven waves in the plasma even at late times. Since $\partial/\partial\theta = \partial/\partial z = 0$, $J_{\text{tot}\,r} = 0$, thus $J_{er} = -J_{ir}$. Note also that $J_{ir} \propto v_{\text{plasma},r}$ goes to zero at the axis and outer wall.

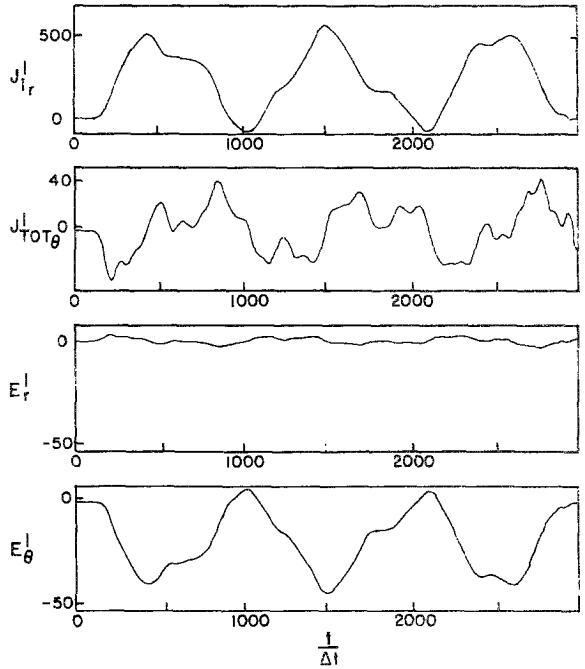

FIG. 12. Quantities in diagnostic cell as functions of time for return current problem: from top to electric field components.

Profiles of the total azimuthal current appear in Fig. 11d. At $t = 12$, the maximum total current density, 4×10^{-4}, is much less than the drive current density maximum of 1.0, and the radially integrated total current is much smaller still. By $t = 500$, the total current density is essentially that of the drive current.

Time histories of various field and current quantities at the "diagnostic cell" location are shown in Fig. 12. Even after 3000 steps, when J_θ (drive) $\simeq 3000$, plasma currents are seen to oscillate without growth. Timescales corresponding to the cyclotron period and the Alfven transit time are evident in the plots.

VI. Conclusion

We have described in detail a linearized, $3D$ hybrid code, and presented evidence of its correct behavior in modeling cold plasma normal modes, and plasma return currents. The methods described are directly applicable to problems involving other geometries, provided only that the equilibrium contain at least one ignorable spatial coordinate, and to a large degree to nonlinear hybrid codes as well. Current applications include the study of precessional modes of infinitely long layers, and studies of axial and radial kink modes of ion rings, both weak and field-reversed. Future applications will employ RINGHYBRID in the study of field-reversed mirror stability.

APPENDIX: Normalization

The code normalization is achieved by choosing the fundamental parameters: $\tau \equiv \Delta t \equiv$ timestep; $\rho \equiv \Delta r \equiv$ radial cell size; $\alpha \equiv \Delta r/\Delta z$, $\Delta z \equiv$ axial cell size; $\mu \equiv$ mass unit of the hot component (normally the porton mass); $e \equiv$ charge unit of the hot component (normally the proton charge), in terms of which the dimensionless code variables, denoted with primes, are related to the (unprimed) physical variables by:

$$
\begin{aligned}
t &= \tau t', & E_z &= (\rho\mu/\alpha\tau^2 e)\, E'_z, \\
r &= \rho r', & B_{r,\theta} &= (\mu c/\alpha\tau e)\, B'_{r,\theta}, \\
z &= (\rho/\alpha)\, z', & B_z &= (\mu c/\tau e)\, B'_z, \\
v_{r,\theta} &= (\rho/\tau)\, v'_{r,\theta}, & A_\theta &= (\rho\mu c/\tau e)\, A'_\theta, \\
v_z &= (\rho/\alpha\tau)\, v'_z, & P_{\theta k}/m_k &= (\rho^2/\tau)\, P'_{\theta k}, \\
E_{r,\theta} &= (\rho\mu/\tau^2 e)\, E'_{r,\theta}. & q_k/m_k &= (e/\mu)\, g'_k,
\end{aligned}
$$

Thus, in the normalized (primed) variables $\Delta r' = \Delta z' = \Delta t' = 1$, and the step sizes never need to be introduced when computing temporal and spatial derivatives (α does appear, however). Note that $\omega_{ck}\tau = g'_k B'$ and, in dimensionless form,

$$
\begin{aligned}
&\dot{\mathbf{r}}'_k = \mathbf{v}'_k\,; \dot{\mathbf{v}}'_k = g'_k(\mathbf{E}' + \mathbf{v}'_k \times \mathbf{B}'); \\
&v'_{\theta k} = P'_{\theta k}/r'_k - g'_k A'_\theta \\
&B'_r = -\alpha^2\, \partial A'_\theta/\partial z', B'_z = (1/r')\, \partial(r' A'_\theta)/\partial r'.
\end{aligned}
$$

To express currents and densities in dimensionless units, we let each simulation particle k represent N_k real particles of mass m_k, charge q_k. The charge and current densities in a cell of radial index j are then

$$n_q = \frac{\sum_k N_k q_k}{2\pi r_j \rho^2/\alpha}, \qquad \mathbf{J} = \frac{\sum_k N_k q_k \mathbf{v}_k}{2\pi r_j \rho^2/\alpha},$$

where the sum is weighted over particles in the cell by charge-sharing. Setting

$$n_q = (\mu c^2/4\pi\rho^2 e)\, n'_q, \qquad \sigma = (\tau c^2/4\pi\rho^2)\, \sigma',$$
$$J_{r,\theta} = (\mu c^2/4\pi\rho\tau e)\, J'_{r,\theta}, \qquad W'_k = (2e\alpha/\mu c^2\rho)\, N_k q_k,$$
$$J_z = (\mu c^2/4\pi\rho\tau\alpha e)\, J'_z,$$

the zero-order field equation, and charge and current densities become

$$\frac{\partial}{\partial r'}\frac{1}{r'}\frac{\partial}{\partial r'}(r' A'_\theta) + \alpha^2 \frac{\partial^2}{\partial z'^2} A'_\theta = -\left(J'_\theta - \sigma'_0 \frac{\partial A'_\theta}{\partial t'}\right),$$

$$n'_q = \frac{\sum_k W'_k}{r_j},$$

$$\mathbf{J}' = \frac{\sum_k W'_k \mathbf{v}'_k}{r_j}.$$

The particle charge appears only through the combinations q_k/m_k and $N_k q_k$, allowing some choice in setting the parameters q_k and N_k. If one assumes e, μ appropriate to a proton and lets $q_k = e$, then N_k turns out to be a large number; alternatively, N_k may be thought of as unity, and then q_k will be the charge of a large number of protons.

The plasma model for the first-order equations requires the introduction of new dimensionless variables. The first-order resistivity η transforms like a reciprocal conductivity, $\eta = (4\pi\rho^2/\tau c^2)\, \eta'$. The background charge density is $n_{qi} = (\mu c^2/4\pi\rho^2 e)\, n'_{qi}$ and, defining the background ion charge and mass as Ze and $m\mu$, respectively, the background number density is given by: $Zn_i = (\mu c^2/4\pi\rho^2 e^2)\, n'_{qi}$, the ion plasma frequency ω_{pi} is defined by $\omega_{pi}^2 = 4\pi n_i Z^2 e^2/m\mu$, from which

$$\omega'^2_{pi} = (Z/m)(c^2\tau^2/\rho^2)\, n'_{qi}.$$

The corresponding Alfvèn velocity v_A is defined by $v_A^2 = c^2\Omega^2/\omega_{pi}^2$, from which $v'^2_A = (Z/m)\, B'^2/n'_{qi}$. Since the plasma frequency does not appear explicitly, the quantity $\rho/\tau c$ need not be specified and c scales out of the problem. We thus introduce the code variables $n'_{qi} \equiv \rho'_i$ and (Z/m).

ACKNOWLEDGMENTS

The authors gratefully acknowledge useful discussions with H. L. Berk, C. K. Birdsall, J. A. Byers, B. I. Cohen, A. T. Drobot, R. L. Ferch, and R. V. E. Lovelace.

The work of A. Friedman and R. N. Sudan was supported by the U.S. Department of Energy under Contracts EY-76-S-02-3170. The work of J. Denavit was supported jointly by the U.S. Department of Energy under Contract EY-76-S-02-2200 and the Office of Naval Research under Contract N00014-75-0473. Acknowledgment is made to the National Magnetic Fusion Energy Computing Center for computer time used in this research; many of the personnel of that organization provided useful assistance with code implementation. During the final preparation of this paper, the work of Alex Friedman was supported at U.C. Berkeley under Contract DEAS03-76SF-00034-DEAT03-76ET53064.

REFERENCES

1. G. MORIKAWA *et al.*, *Phys. Fluids* **12** (1969), 1648; M. N. BUSSAC, H. P. FURTH, AND M. N. ROSENBLUTH, *in* "Proc. of the 7th Int. Conf. on Plasma Physics and Controlled Nuclear Fusion Research" (Innsbruck, Austria, 1978), Paper CN37/X-1.
2. See for example, A. G. ESKOV *et al. in* "Proc. 7th European Conf. on Controlled Fusion and Plasma Physics," Lausanne, Switzerland, 1975, Vol. I, p. 55.
3. W. C. CONDIT, JR., T. K. FOWLER, AND R. F. POST, Lawrence Livermore Laboratory Report UCRL-58002, Feb. 1977.
4. J. W. SHEARER, J. L. EDDLEMAN, C. W. HARTMAN, AND W. C. TURNER, *Bull. Amer. Phys. Soc.* **23** (1978), 910.
5. N. C. CHRISTOFILOS, *Proc. 2nd* UN *Int. Conf. on Peaceful Uses of Atomic Energy* **32** (1958), 279.
6. R. N. SUDAN AND E. OTT, *Phys. Rev. Lett.* **33** (1974), 355.
7. H. H. FLEISCHMANN AND T. KAMMASH, *Nucl. Fusion* **15** (1975), 1143.
8. J. J. BZURA, T. J. FESSENDEN, H. H. FLEISCHMANN, D. A. PHELPS, A. C. SMITH, AND D. M. WOODALL, *Phys. Rev. Lett.* **29** (1972), 256.
9. S. HUMPHRIES, J. J. LEE, AND R. N. SUDAN, *Appl. Phys. Lett.* **25** (1974), 20; R. N. SUDAN, *in* "Proc. 8th European Conf. on Controlled Fusion and Plasma Physics," Prague, Czechoslavakia, 1977, Vol. 2, p. 191; J. GOLDEN AND C. KAPETANAKOS, *Appl. Phys. Lett.* **28** (1976), 3.
10. P. L. DREIKE, D. A. HAMMER, R. N. SUDAN, AND L. WILEY, *Phys. Rev. Lett.* **41** (1978), 1328.
11. M. J. GERVER AND R. N. SUDAN, *Phys. Fluids* **22** (1979), 686.
12. H. L. BERK AND R. N. SUDAN, *J. Plasma Phys.* **6** (1971), 413.
13. R. V. E. LOVELACE, *Phys. Fluids* **22** (1979), 708.
14. K. D. MARX, *Phys. Fluids* **11** (1968), 357.
15. R. V. E. LOVELACE, *Phys. Fluids* **21** (1978), 1389.
16. J. L. JOHNSON, R. M. KULSRUD, AND K. E. WEIMER, *Plasma Phys.* **11** (1969), 463.
17. R. V. E. LOVELACE, *Phys. Fluids* **19** (1976), 723.
18. R. N. SUDAN AND M. N. ROSENBLUTH, *Phys. Rev. Lett.* **36** (1976), 972.
19. B. MARDER AND H. WEITZNER, *Plasma Phys.* **12** (1970), 435.
20. D. V. ANDERSON, J. KILLEEN, AND M. E. RENSINK, *Phys. Fluids* **15** (1972), 351.
21. J. M. FINN AND L. SPARKS, Cornell Univ. Lab. of Plasma Studies Report 230, 1977.
22. J. A. BYERS, *in* "Proc. 4th Conf. on Numerical Simulation of Plasmas," 1970, p. 496.
23. O. BUNEMAN, *in* "Proc. 7th Conf. on Numerical Simulation of Plasmas," 1975, p. 102.
24. A. FRIEDMAN, R. L. FERCH, R. N. SUDAN, AND A. T. DROBOT, *Plasma Phys.* **19** (1977), 1101.
25. A. MANKOFSKY, A. FRIEDMAN, AND R. N. SUDAN, Cornell Univ. Lab. of Plasma Studies Report 245, 1978, to appear in *Plasma Phys.*
26. J. P. BORIS, *in* "Proc. 4th Conf. on Numerical Simulation of Plasmas," 1970, p. 4.

27. D. L. BOBROFF. *IRE Trans. Electron Devices*, **ED-6** (1959). In a private communication, J. A. Byers notes that Bobroff's "polarization variables" are immediately applicable to linearized simulation.
28. A. FRIEDMAN AND R. N. SUDAN, Cornell Univ. Lab. of Plasma Studies Report 237, 1978.
29. J. A. BYERS, B. I. COHEN, W. C. CONDIT, AND J. D. HANSON, *J. Comput. Phys.* **27** (1978), 363.
30. I. B. BERNSTEIN AND S. K. TREHAN, *Nucl. Fusion* **1** (1960), 3.
31. T. H. STIX, "The Theory of Plasma Waves," McGraw–Hill, New York, 1962, p. 82.
32. H. L. BERK AND L. D. PEARLSTEIN, *Phys. Fluids* **19** (1976), 1831.
33. W. C. CONDIT, Lawrence Livermore Laboratory Report UCID-17683, 1977.